Differential medial temporal lobe and default-mode network functional connectivity and morphometric changes in Alzheimer's Disease

Kamil A. Grajski[1] and Steven L. Bressler[2], for the Alzheimer's Disease Neuroimaging Initiative[3]

Correspondence to: Dr. Kamil A. Grajski,
NuroSci, LLC.,
525 South Flagler Drive,
Suite 21CD, West Palm Beach,
FL, 33401,

E-mail: kgrajski@nurosci.com

Abstract

We report group level differential detection of medial temporal lobe resting-state functional connectivity disruption and morphometric changes in the transition from cognitively normal to early mild cognitive impairment in an age-, education- and gender-matched 105 subjects Alzheimer's Disease Neuroimaging Initiative dataset. In mild Alzheimer's Disease, but not early mild cognitive impairment, characteristic brain atrophy was detected in FreeSurfer estimates of cortical thickness and subcortical and hippocampal subfield volumes. By contrast, functional connectivity analysis detected earlier significant changes. In early mild cognitive impairment these changes involved medial temporal lobe regions of transentorhinal, perirhinal and entorhinal cortices (associated with the earliest stages of

[1] NuroSci, LLC. West Palm Beach, FL, 33401.
[2] Center for Complex Systems and Brain Science, Florida Atlantic University, Boca Raton, FL, 33431.
[3] Data used in preparation of this article were obtained from the Alzheimer's Disease Neuroimaging Initiative (ADNI) database (adni.loni.usc.edu). As such, the investigators within the ADNI contributed to the design and implementation of ADNI and/or provided data but did not participate in analysis or writing of this report. A complete listing of ADNI investigators can be found at: http://adni.loni.usc.edu/wp-content/uploads/how_to_apply/ADNI_Acknowledgement_List.pdf.

neurofibrillary changes in Alzheimer's Disease), hippocampus, parahippocampal gyrus and temporal pole, and cortical regions comprising or co-activated with the default-mode network, including rostral and medial prefrontal cortex, anterior cingulate cortex, precuneus and inferior temporal cortex. Key findings include: a) focal and bilaterally symmetric spatial organization of affected medial temporal lobe regions; b) mutual hyperconnectivity bilaterally involving ventral medial temporal lobe structures (temporal pole, uncus); and c) dorsal medial temporal lobe hypoconnectivity with anterior and posterior midline default-mode network nodes. These findings position medial temporal lobe resting state functional connectivity as a candidate biomarker of an Alzheimer's Disease pathophysiological cascade, potentially in advance of clinical biomarkers, and coincident with biomarkers of the earliest stages of Alzheimer's neuropathology. Our results indicate that medial temporal lobe resting-state functional connectivity should be further investigated as a potential biomarker in the diagnosis of Alzheimer's Disease.

Highlights

- Functional connectivity change seen before structural change in Alzheimer's Disease
- Medial temporal lobes mutually hyper-connect in mild cognitive impairment
- Medial temporal lobe and default mode network decouple in mild cognitive impairment
- Loci of functional change in hippocampi are focal with bilaterally symmetric features
- Nonmonotonic functional connectivity changes in Alzheimer's Disease progression

Keywords: hippocampus; medial temporal lobe; hyperconnectivity; hypoconnectivity

Abbreviations: ADNI = Alzheimer's Disease Neuroimaging Initiative; CA = cornu ammonis; CDR = clinical dementia rating; CDRSB = clinical dementia rating, sum of boxes; CDT = cluster determination threshold; CN= cognitively normal; CSF = cerebrospinal fluid; D = dementia;

DMN = default-mode network; EPI = echo-planar image; FWHM = full width half maximum; ICA = independent components analysis; ICV = intra-cranial volume; MCI = mild cognitive impairment; MMSE = mini-mental state examination; MTL = medial temporal lobe; PCC = posterior cingulate cortex; PHG = parahippocampal gyrus; rsfMRI = resting-state functional MRI; ROI = region of interest;

Running Title: Alzheimer's Disease medial temporal lobe functional connectivity and morphometric changes

1. Introduction

In late-onset Alzheimer's Disease, neuropathologies may cumulate for decades before possible though not inevitable clinical manifestation. Diagnostic guidelines (Albert, 2011; Jack, 2011a; McKhann, 2011; Sperling, 2011) and a research framework (Jack, et al., 2018) for cognitively normal (CN), mild cognitive impairment (MCI), and Alzheimer's Disease individuals, consider multiple neuroimaging modalities including amyloid β and tau tracers, markers of metabolic activity (FDG PET), and morphometry (MRI). An hypothesized Alzheimer's Disease pathophysiological cascade links these neuroimaging modalities together with cerebrospinal fluid (CSF) markers for amyloid β and tau to the Alzheimer's Disease clinical progression (Jack, 2011b, 2013).

The hypothesis tested in this investigation was that functional connectivity disruption can be detected in the early MCI group. Disruption of functional connectivity in Alzheimer's Disease has been observed in the default-mode network and other resting-state networks in resting-state functional MRI (rsfMRI) (Greicius, et al., 2004; Buckner, et al., 2005; Sorg, et al., 2007; Sperling, et al., 2010; Zhou, et al., 2010; Jones, et al., 2011; Jones, et al., 2012, 2016; Brier, et

71 al., 2012; Ward, et al., 2014; Cai, et al., 2015; Dillen, et al., 2017). However, such observations
72 have not broadly impacted clinical practice (Woo, et al., 2017).

73 The purpose of the present study is thus to compare functional biomarkers using functional
74 connectivity analysis of resting-state fMRI, with structural imaging biomarkers serving as a
75 reference baseline. The experimental design is a group-level analysis of an Alzheimer's Disease
76 Neuroimaging Initiative (ADNI) population containing clinically-defined cognitively normal,
77 early MCI and mild Alzheimer's dementia subgroups. We observed cortical thinning,
78 subcortical volume loss, and whole hippocampal and hippocampal subfield volume loss, in the
79 mild Alzheimer's Disease subgroup, but not in the early MCI group. A group-level pairwise
80 region of interest (ROI) analysis was used to assess functional connectivity changes. *A priori*,
81 the first element in each ROI pair (the "anchor ROI") was in the medial temporal lobe (MTL)
82 identified by a method described below. The reason to anchor each ROI pair in the MTL was
83 that it is in the MTL perirhinal cortex (Brodmann Areas 35 and 36) and, specifically, the
84 transentorhinal region (Brodmann Area 35) that the neurofibrillary changes associated with
85 Alzheimer's Disease start and then, in a progression with disease stages, appear in entorhinal
86 cortex (Brodmann Area 28), hippocampus and temporal cortex, association cortices, and
87 ultimately primary sensory cortices (Braak and Braak, 1985, 1991). The ROI position of the
88 second element in each identified ROI pair was determined in a data-driven method described
89 below. The combination of *a priori* and data-driven approach directly linked functional
90 connectivity analysis to focal regions of earliest neuropathology in Alzheimer's Disease.

91 We report evidence that functional connectivity changes occur in the CN to early MCI transition
92 in the absence of structural imaging findings. The progression of observed CN to MCI
93 functional connectivity changes was further evaluated by comparing the mild Alzheimer's

Disease and CN groups. We conclude that rsfMRI functional connectivity analysis of MTL may provide a complementary approach to established neuroimaging and other biomarkers within a model of Alzheimer's Disease pathophysiology (Jack, 2013) and an Alzheimer's Disease research framework (Jack, et al., 2018).

2. Materials and Methods

Data used in the preparation of this report were obtained from the Alzheimer's Disease Neuroimaging Initiative (ADNI) database (adni.loni.usc.edu). The ADNI project was launched in 2003 as a public-private partnership, led by Principal Investigator Michael Weiner, MD. The primary goal of ADNI has been to test whether serial magnetic resonance imaging, positron emission tomography, other biological markers, and clinical and neuropsychological assessment can be combined to measure the progression of mild cognitive impairment and early Alzheimer's Disease.

2.1. Participants

The participants in this report were a subset of the ADNI 2 experimental sub-study on resting state fMRI functional connectivity (rsfMRI) (Jack, et al., 2008; Weiner, et al., 2015). The ADNI 2 rsfMRI studies available for download on the Laboratory of Neuro Imaging (LONI) website in September 2016 consisted of 886 scan pairs (structural MRI, rsfMRI) from 220 participants. We subjected scans to a rigorous multistage preprocessing and quality assurance procedure described in further detail below and summarized in Supplemental Figure 1. The procedure yielded a 105 participants cross-sectional study dataset.

114 Table 1 summarizes participant demographics and metadata. Participants were assigned to one
115 of three clinical categories: CN; early MCI; and mild Alzheimer's Disease. Clinical assignments
116 adhered to ADNI 2 protocols (publicly available on the adni.loni.usc.edu website). The three
117 clinical groups were balanced for age ($P = 0.56$), education ($P = 0.95$) and gender ($P = 0.22$).
118 The effect of clinical group was significant for Clinical Dementia Rating (CDR) ($P < 0.001$),
119 Clinical Dementia Rating Sum-of-Boxes (CDR-SB) ($P < 0.001$), Mini-Mental State
120 Examination (MMSE) ($P < 0.001$), and APOEε4 ($P = 0.007$).

121 **Table 1.** Study participant demographics and metadata.

	CN n = 32	**MCI n = 39**	**AD n = 34**	**P value**
Age (Mean, SD)	74.2 (5.5)	72.5 (6.8)	73.4 (7.2)	0.56[(b)]
Female (n, %)	18 (56)	22 (56)	13 (38)	0.22[(a)]
Education (Mean, SD)	16 (2.2)	16 (2.5)	17 (2.6)	0.95[(b)]
CDR (Median, Min, Max)	0 (0, 0)	0.5 (0.5, 0.5)	0.5 (0.5, 1.0)	<0.001[(b)]
CDR-SB (Median, Min, Max)	0 (0, 0)	1.0 (0.5, 3.0)	2.5 (0.5, 7.0)	<0.001[(b)]
MMSE (Median, Min, Max)	29.5 (27, 30)	29 (27, 30)	25 (20, 26)	<0.001[(b)]
APOEε4=2 (n, %)	1 (3)	4 (10)	9 (26)	0.007[(a)]

[a](Chi-square test); [b](ANOVA);
AD = Alzheimer's Disease; CDR = clinical dementia rating; CDR-SB = clinical dementia rating sum-of-boxes, CN = cognitively normal; MCI = mild cognitive impairment; MMSE = mini-mental state examination; SD = standard deviation;

122

123 *2.2. Image acquisition*

124 The present analysis focuses on two of the up to eight scans obtained during a typical ADNI 2
125 subject visit. These are the high-resolution T_1-weighted 3D whole brain structural scan (Scan #2
126 in the protocol) and the resting state functional scan (Scan #4 in the protocol). Structural and
127 rsfMRI scans were acquired with 3T MRI scanners of a single manufacturer (Philips Medical

128 Systems: Achieva, Ingenia, Ingenuity, Intera) from 14 unique sites in two configurations
129 (MULTI-COIL; SENSE-HEAD), and fifteen (15) different software versions (3.2.1 or higher).
130 Structural scans were acquired with a T_1-weighted sagittal magnetization-prepared rapid gradient
131 echo (MP-RAGE) sequence, with 1.2 mm right/left, 1.0 mm anterior/posterior and 1.0 mm
132 superior/inferior resolution. RsfMRI scans were acquired with a T_2-weighted gradient echo
133 planar imaging sequence with repetition time/echo time, 3000/30, flip angle, 80°, 48 axial slices,
134 and 64 x 64 in-plane matrix yielding an isotropic 3.3 mm voxel size. Phase-directions varied:
135 anterior-posterior, N = 16; posterior-anterior, N = 86; missing values = 4. Only two temporal
136 slice order sequences were included in this study dataset: a) ascending 48 planes (odd, even),
137 N=98; and b) descending 48 planes (even, odd), N=7. RsfMRI scans were of two durations: a)
138 140 TRs ("resting state", N=91); and b) 200 TRs ("extended resting state", N=14). Additional
139 image acquisition protocol details can be found on the public adni.loni.usc.edu website.

140 *2.3. Image processing*

141 Structural images and rsfMRI images were downloaded from LONI either in DICOM format
142 (and locally converted using dcm2nii) or in 4DNIfTI format (DICOM to NIfTI conversion
143 performed by LONI). Preprocessing and data analysis were performed using a combination of
144 FreeSurfer (Dale, et al., 1999), Analysis of Functional Neuroimages (AFNI) (Cox, 1996), and
145 "home-grown" analysis implemented in R and *tcsh* shell scripts. The AFNI Version was
146 AFNI_17.1.03 (2-May-2017). The FreeSurfer version was V6.0 run in the Amazon Cloud on
147 Ubuntu 14.04. The R version was Version 3.4.3 (30-Nov-2017). The AFNI Python script
148 uber_subject.py was used to generate a preprocessing shell script which was manually edited.

149 *Structural image analysis with FreeSurfer 6.0*

150 Subcortical and hippocampal subfield segmentation, and cortical parcellation (surface area,
151 thickness and volume) were obtained with FreeSurfer Version 6.0 image analysis suite, which is
152 documented and freely available for download online (http://surfer.nmr.mgh.harvard.edu/) (Dale,
153 et al., 1999). FreeSurfer default settings were applied via the "recon-all" command.

154 *Functional MRI analysis with AFNI*

155 The rsfMRI echo-planar image (EPI) preprocessing sequence consisted of the following steps
156 using AFNI: a) alignment of EPI centers to a standard atlas (MNI_avg152T1); b) elimination of
157 the first ten (10) EPIs; c) outlier detection and de-spiking; d) application of time-shift correction;
158 e) alignment to the least motion distorted volume; f) alignment to the anatomical image and warp
159 to a standard space (MNI_avg152T1); g) generation of anatomical and EPI masks; h) application
160 of spatial smoothing (FWHM = 4.0mm); i) scaling voxel time series to a mean of 100; j)
161 generation of demeaned motion parameters and motion parameter derivatives; k) generation of
162 motion "censor" masks (motion limit = 0.3); l) generation of ventricle (Vent) and white-matter
163 (We) segmentation masks from FreeSurfer segmentation and parcellation results; and m)
164 deconvolution with 12 regressors (6 regressors + 6 motion derivatives). The process yielded a
165 4D residual error volume that served as input to the next stage of volumetric and correlation
166 analysis. Global signal regression (GSR) was not performed. Bandpass filtering was performed
167 in the final ROI pairwise analysis stage as discussed below.

168 Table 2 lists pre-processing stage group-level statistical summaries obtained from AFNI
169 *@ss_review_basic*. There were no significant differences between groups for average censored
170 motion, maximum censored motion and the average fraction of TR frames censored for excess

171 motion. Group average temporal signal-to-noise values were in excess of 170 with standard
172 deviation in the range 16-19, indicating good overall input EPI signal levels. The values did not
173 differ significantly across groups. Finally, the group average Dice coefficient, which measures
174 the extent of overlap between the anatomical and EPI brain masks, was in excess of 0.88 with
175 standard deviation in the range, 0.012-0.015, indicating good overall anatomical – EPI
176 alignment. The values did not differ significantly across groups.

177 **Table 2.** Group-average pre-processing statistics.

	CN n = 32	**MCI n = 39**	**AD n = 34**	**P value[(a)]**
Avg. Censored Motion (Mean, SD)	0.095 (0.02)	0.091 (0.02)	0.091 (0.02)	0.63
Max. Censored Motion (Mean, SD)	0.473 (0.11)	0.508 (0.13)	0.506 (0.14)	0.46
Censor Fraction (Mean, SD)	0.09 (0.06)	0.08 (0.06)	0.10 (0.07)	0.56
Avg. TSNR (Mean, SD)	179 (16)	178 (19)	180 (16)	0.85
Global Correlation (Mean, SD)	0.022 (0.01)	0.022 (0.01))	0.023 (0.01)	0.91
Dice Coefficient (Mean, SD)	0.888 (0.01)	0.891 (0.02)	0.890 (0.01)	0.69

[a] *(ANOVA);* AD = Alzheimer's Disease; CDR = clinical dementia rating; CDR-SB = clinical dementia rating sum-of-boxes, CN = cognitively normal; MCI = mild cognitive impairment; SD = standard deviation; TSNR = temporal signal-to-noise.

178

179 *2.4. Image quality assurance*

180 The initial database consisted of 886 rsfMRI scans (and their paired structural images) from 220
181 subjects. An R package "ADNIMERGE" contained MRI and rsfMRI quality assessments (e.g.,
182 comments by ADNI quality reviewers) and related data (e.g., rsfMRI slice order) stored in the
183 tables "mayoadirl_mri_imageqc" and "mayoadirl_mri_fmri", respectively. The 886-scan set was
184 reduced to 673 scans (n=196) by rejecting all scans that did not conform to the slice order
185 sequences listed above, or failed visual inspection in the FSL viewer, or contained any reviewer

comment in either of the available pair of comment fields. Comments typically referenced motion or clinical findings.

The rsfMRI EPI preprocessing sequence, with motion-limit set to 0.3, was applied to each of the 673 structural-rsfMRI pairs. The global signal was analyzed as an initial screen for excessive motion. Scans were rejected if the global average time-series amplitude value fell outside the range 96-104 or if the standard deviation of the global average time series exceeded 2.0. This gross motion screening procedure reduced the analysis database to 507 structural-rsfMRI pairs (n=190 subjects).

The 507 scan pairs database was further screened using statistics generated by the AFNI-based preprocessing pipeline. Scans were marked for rejection according to the following criteria: a) DICE coefficient < 0.78; b) censor fraction > 0.21; c) maximum censored displacement > 1.00; d) average TSNR > 400 or average TSNR < 100; e) degrees of freedom left < 100; and f) global correlation < 0.10. 206 scan pairs from 106 subjects met these quality assurance criteria. Where multiple candidate scan pairs were present for a given subject, the latest available pair was selected. 80% of the final dataset consisted of scans obtained from subjects who were on at least their second ADNI 2 study visit. The final study database consisted of 105 structural-functional scan pairs from 105 subjects. ANOVA confirmed that preprocessing quality measures were matchead across the three diagnostic groups. See Table 2.

2.5. ROI seed and ROI pairs of interest identification

ROI seeds for ROI pairwise functional connectivity analysis were identified by an hybrid *a priori data-driven* method. The procedure was applied independently in left and right hemispheres. To bootstrap the ROI seed selection procedure, FreeSurfer subcortical

208 segmentations were used to define the global 3D bounding box for the hippocampus and MTL.
209 A grid of 6mm-spaced coordinates within the bounding box formed the input candidate ROI seed
210 pool. Input candidate seeds were retained subject to the conditions that the mask for a 6mm
211 radius spatial sample (33 voxels) centered on the ROI seed was 100% contained within the
212 global anatomical brain mask, and not greater than 50% overlap with either of the global
213 ventricle or global white matter masks obtained during pre-processing. The qualifying set of
214 6mm radius input ROI masks were summed (AFNI *3dMask*) and visually inspected
215 (Supplemental Figure 2). For each subject and for each input ROI mask, the average time series
216 was computed and retained using AFNI *3dmaskave*.

217 To obtain candidate ROI pairs for analysis, we performed for each input candidate ROI the
218 following group-level procedure. First, the average time series computed and stored in the
219 preceding step, was used to compute the Fisher z-transformed Pearson correlation coefficient
220 with every other voxel in the subject 4D image (AFNI *3dfim+*). Computation was restricted to
221 those voxels contained within the global brain mask generated during AFNI baseline
222 processing). Second, a group-level, one-way, three-factor (CN, MCI, Dementia) 3D ANOVA
223 (AFNI *3dAnova*) was conducted and the 3D volume of F statistics was retained. Third, a 3D
224 cluster analysis (AFNI *3dclust*) was performed on the F statistic 3D volume and for each
225 qualifying cluster a candidate ROI mask of a 6mm spatial sample located at the cluster center of
226 mass was retained. Qualifying clusters were those with threshold F-statistic ($F \geq 3.086$; $p \leq 0.05$,
227 uncorrected) and minimum cluster size ($N_C = 20$). These parameters were permissive by design.
228 Fourth, only those candidate ROIs were retained for which the mask was 100% contained within
229 the global brain mask (not including the brainstem and cerebellum) and did not have greater than
230 50% overlap with either the global ventricle or global white matter masks. Fifth, qualifying

candidate ROI masks were visually inspected. Sixth, the ROI seed list was pruned to retain only those MTL ROI seeds (the anchor ROIs in ROI pairs of interest) that generated candidate ROIs through the F-statistical map analysis. Finally, individual subject average time series for the final F-statistic map-driven ROI masks were computed and stored.

The above ROI identification procedure yielded ROI "pairs of interest" in which the anchor element in each ROI pair was a left (right) hemisphere MTL ROI. The second element (non-anchor) in each ROI pair was the corresponding F-statistic map-driven ROI whose position was determined by the data. For example, in an ROI pair of interest whose anchor element was in left MTL, the position of the second ROI could lie in ipsilateral or contralateral hemisphere, including MTL. For the left hemisphere, 22 MTL ROI seeds formed the anchor MTL element in 50 ROI pairs of interest (see Supplemental Figure 3). For the right hemisphere, 38 MTL ROI seeds formed the anchor MTL element in 82 ROI pairs of interest (see Supplemental Figure 4). A cluster analysis (AFNI *3dclust*) of the sum of non-anchor ROI masks showed that they comprised a restricted subset of brain regions. For left hemisphere, there were 31 clusters with a maximum of three ROI masks in overlapping anatomical positions. For right hemisphere, there were also 31 clusters with a maximum of five ROI masks in overlapping anatomical positions. Findings in the present study described in detail below are with respect to these anchor MTL and non-anchor ROI pairs of interest.

2.6. ROI time series quality assurance

Individual ROI residual time series were band-pass filtered (4th order Butterworth, $f = \{0.01, 0.1\}$) and averaged, and a subjected to a final quality assurance check for outliers. The 3rd-130th (of the original 140 or 200 TRs) time series elements were retained as the candidate final ROI

time series. A subject ROI time series was excluded from group-level analysis if any of the following conditions were true: a) the time series was constant; b) the time series standard deviation, $\sigma > 20.0$; or c) the fraction of time points with values greater than the outlier threshold θ exceeded 5%. The outlier threshold was set as $\theta = \mu + 3\sigma$, where μ was the time series average value.

2.7. ROI pairwise correlation analysis

ROI pairs were subjected to group-level correlation analysis and ANOVA. The core statistical method was one-way, three-factor (clinical group) ANOVA, with *post hoc t* tests applied pairwise (between factors) only for significant ANOVA tests. Correction for large-scale multiple testing was implemented through False Detection Rate (FDR) correction (Benjamini & Hochberg, 1995) and permutation repeated measures (N = 5000) (Nichols and Holmes, 2002; Efron, 2010; Eklund, et al., 2016).

2.8. Assignment of anatomical position to an ROI coordinate

ROI seed coordinates were mapped to anatomical locations by analyzing the output of the AFNI *whereami* output. The AFNI *whereami* tool maps an input coordinate to anatomical position with respect to a multiplicity of atlases. To assign an anatomical label we used the "Focus Point", and "Within 2mm" or "Within 4mm" outputs from the Talairach-Tournoux, MNI (Macro Labels, N27), and MNI (Cytoarchitectonic Max Probability Maps) and checked for consistency. Results were visually confirmed.

3. Results

3.1. Cortical thinning in group-level AD-CN and AD-MCI contrasts, but not in the MCI-CN contrast

The effect of clinical category on cortical thinning was evaluated using one-way, three-factor ANOVA on estimates of cortical thickness from 34 cortical regions per hemisphere (68 total) (Supplemental Table 1; Supplemental Figure 5). An FDR corrected (*q=0.1, N=68 tests*) ANOVA F statistic critical *p* value threshold, $p_F^* = 0.032$, identified 23 significant tests. For significant ANOVA tests only, *post hoc* pairwise *t* tests were computed and FDR-corrected (*q=0.1, N=23 tests*) per contrast and gave critical *p* value thresholds: MCI-CN ($p_{MCI,CN}^*$=0.006); AD-CN ($p_{D,CN}^*$=0.037); and AD-MCI ($p_{D,MCI}^*$=0.022). There were twenty-one significant AD-MCI comparisons and fifteen significant AD-CN comparisons. Effect sizes, measured by Cohen's *d*, were in the range $0.6 \leq d \leq 1.0$. There were two significant positive MCI-CN comparisons (left and right paracentral lobule). All AD-MCI and AD-CN contrasts were negative. There were no significant negative MCI-CN comparisons.

3.2. Subcortical volume changes in group-level AD-CN and AD-MCI contrasts, but not in the MCI CN contrast

The effect of clinical category on subcortical volumes was evaluated using one-way, three-factor ANOVA on estimates of subcortical volumes from 8 cortical regions per hemisphere (16 total) (Supplemental Table 2; Supplemental Figure 5). An FDR-corrected (*q*=0.1*, N=16 tests*) one-way three-factor ANOVA F statistic *p* value, p_F^* = 0.012, identified eight significant tests. For the significant ANOVA tests only, *post hoc* pairwise *t* tests were computed and FDR-corrected

(q=0.1, *N=8 tests*) per contrast: AD-CN ($p^*_{D,CN}$ = 0.004); and AD-MCI ($p^*_{D,MCI}$ = 0.031). There were eight significant AD-CN contrasts; and six significant AD-MCI contrasts. Cohen's d values were in the range $0.3 \leq d \leq 1.1$. All significant pairwise comparisons for ventricles (e.g., inferior lateral ventricle) were positive and all significant pairwise contrasts for subcortical structures (e.g., whole hippocampus) were negative. With an FDR rate q = 0.1, by design set to be liberal, no p value fell below the FDR-corrected value (*N=8 tests*) in the MCI-CN contrast, which indicated no significant MCI-CN comparisons.

3.3. Hippocampal subfield volume reduction in group-level AD-CN and AD-MCI contrasts, but not the MCI-CN contrast

Hippocampal subfields (11 per hemisphere) were analyzed similarly as above and all twenty-two ANOVA tests were significant, FDR corrected p value (*q=0.1, N=22 tests*), p^*_F = 0.032 (Supplemental Table 3). *Post hoc* pairwise t tests detected twenty-two significant AD-CN comparisons ($p^*_{D,CN}$ *= 0.029, N=22 tests*), and eighteen significant AD-MCI comparisons ($p^*_{D,MCI}$ *= 0.077, N=22 tests).* Effect sizes, measured as Cohen's d, were at least "strong" and above, with left hemisphere effect scores uniformly higher than the right hemisphere (left: $0.9 \leq d \leq 1.1$; right: $0.7 \leq d \leq 0.86$). All significant AD-MCI and AD-CN hippocampal sub-field pairwise contrasts were negative. For the MCI-CN contrast no p value was below the FDR-corrected value (*q=0.1, N=22 tests*).

3.4. Significant pairwise ROI functional connectivity changes in the MCI-CN group-level contrast

The effect of clinical category on group average ROI pairwise functional connectivity was evaluated using one-way, three-factor ANOVA in separate analyses for the left hemisphere (50

ROI pairs of interest comprising 50 hypotheses, or simultaneous tests) and for the right hemisphere (82 ROI pairs of interest comprising 82 simultaneous tests). For the left hemisphere, an FDR-corrected (q=0.05*, N=50 tests*) ANOVA F statistic critical p value threshold, p_F^* = 0.026, identified 28 significant tests (Supplemental Table 4). For the significant ANOVA tests only, *post hoc* pairwise t tests were computed and FDR-corrected (q=0.05*, N=28 tests*) independently per contrast: MCI-CN ($p_{MCI,CN}^*$ = 0.0168); AD-CN ($p_{D,CN}^*$ = 0.0214); and AD-MCI ($p_{D,MCI}^*$ = 0.0364). Of the 28 significant ANOVA comparisons, there were ten significant *post hoc* MCI-CN t test comparisons (*post hoc* pairwise t test $p < p_{MCI,CN}^*$). Results are summarized in Table 3. Six of the ten MCI-CN comparisons were positive (indicating hyperconnectivity) with Cohen's effect size d, $0.52 \leq d \leq 0.92$. Four of the ten were negative (indicating hypoconnectivity) with Cohen's d, $0.52 \leq d \leq 0.79$.

Table 3. Left MTL ROI - ROI pairwise significant MCI - CN comparisons[4].

		ANOVA (1-way, 3-levels)						MCI-CN		AD-CN		AD-MCI	
Anatomical Region(s)		FDR p^* = 0.026, q = 0.05, n = 50			Group Average Fisher Z Value			FDR p^* =0.0168		FDR p^* =0.0214		FDR p^* =0.0364	
MTL ROI	ROI	F	p	p^*	CN	MCI	AD	p	d	p	d	p	d
ROI pair hyper-connectivity MCI vs CN													
L: Uncus, A36, Hipp (EC)	L: A38	11.3*	0.00004	0.0000	-0.03	0.18	0.24	**<0.001**	**0.92**	**<0.001**	**1.09**	0.1488	0.25
L: Hipp (CA, FD)	R: A38	8.7	0.00034	0.0010	0.05	0.13	0.23	**0.0156**	**0.52**	**<0.001**	**1.01**	**0.0138**	**0.52**
L: A35, A36, Hipp (SUB, CA)	R: Uncus, A28, A36	7.0*	0.00145	0.0018	-0.04	0.14	0.04	**<0.001**	**0.83**	0.0406	0.42	**0.0162**	**0.51**
L: Hipp (CA)	R: A10, A47	6.3	0.00252	0.0032	-0.08	0.05	-0.08	**0.0016**	**0.66**	0.4716	0.02	**0.0006**	**0.80**
L: A27, Hipp (FD, CA, SUB)	R: A10, A11	5.6	0.00489	0.0056	0.00	0.08	-0.04	**0.0168**	**0.52**	0.1380	0.27	**0.0012**	**0.74**
L: Uncus, A36, A28, Hipp (SUB)	L: A34	4.4	0.01515	0.0188	-0.06	0.08	0.06	**0.0042**	**0.65**	**0.0096**	**0.57**	0.3524	0.09
ROI pair hypo-connectivity MCI vs CN													
L: Hipp (FD, CA, SUB), Ling. G.	L+R: Precuneus	5.8	0.00424	0.0040	0.20	0.05	0.09	**0.0002**	**0.79**	**0.0050**	**0.63**	0.2098	0.19
L: A35, A36, Hipp (SUB, CA)	L+R: Precuneus	4.6	0.01187	0.0122	0.21	0.08	0.10	**0.0034**	**0.68**	**0.0142**	**0.56**	0.3586	0.09
L: A28, A35, Hipp (SUB, EC, CA)	R: A45, A47	4.5	0.01291	0.0104	0.08	-0.05	0.07	**0.0098**	**0.58**	0.4490	0.04	**0.0040**	**0.64**
L: Caudate tail, Hipp (CA, FD)	L+R: ACC	3.8	0.02570	0.0260	0.12	0.01	0.06	**0.0016**	**0.71**	0.0622	0.38	0.1258	0.27

ACC = anterior cingulate cortex; AD = Alzheimer's disease; CA = cornu ammonis; CN = cognitively normal; EC = entorhinal cortex; FD = dentate gyrus; FDR = false detection rate; Hipp = hippocampus; Ling. G. = lingual gyrus; MCI = mild cognitive impairment; MTL = medial temporal lobe; ROI = region of interest; SUB = subiculum; *(Significant at FDR q = 0.01).

For the right hemisphere, an FDR-corrected (q=0.05*, N=82 tests*) ANOVA F statistic critical p value threshold, p_F^* = 0.0102, identified 17 significant MCI-CN comparisons (Supplemental Table 5). For the significant ANOVA tests only, *post hoc* pairwise t tests were computed and

[4] Supplemental Information Table 6 (Worksheet MCI-CN_Detail) provides additional details, including ROI MNI coordinates.

FDR-corrected (q=0.05, *N=17 tests*) independently per contrast: MCI-CN ($p^*_{MCI,CN}$ = 0.027); AD-CN ($p^*_{D,CN}$ = 0.0034); and AD-MCI ($p^*_{D,MCI}$ = 0.0278). Of the 17 significant ANOVA comparisons, there were 13 significant *post hoc* MCI-CN *t* test comparisons (*post hoc* pairwise *t* test $p < p^*_{MCI,CN}$). Results are summarized in Table 4. Nine of the 13 MCI-CN comparisons were positive (indicating hyperconnectivity) with Cohen's effect size d, $0.45 \leq d \leq 0.95$. Four of the 13 were negative (indicating hypoconnectivity) with Cohen's d, $0.57 \leq d \leq 0.73$.

Table 4. Right MTL ROI - ROI pairwise significant MCI - CN comparisons[5].

		ANOVA (1-way, 3-levels)						MCI - CN *post hoc t* tes		AD - CN *post hoc t* test		AD - MCI *post hoc t* tes	
Anatomical Region(s)		FDR p^* = 0.0102, q = 0.05, n = 81			Group Average Fisher Z Value			FDR p^* =0.027		FDR p^* =0.003		FDR p^* =0.028	
MTL ROI	ROI	F	*p*	*p**	CN	MCI	AD	*p*	*d*	*p*	*d*	*p*	*d*
ROI pair hyper-connectivity MCI vs CN													
R: Uncus, A28, Hipp (CA, SUB)	L: Uncus, EC, A38	11.6*	0.00003	0.0000	-0.12	0.04	0.05	**0.0000**	**0.95**	**0.0000**	**1.14**	0.4620	0.02
R: A36, Hipp (CA, FD)	R: A9, A10	8.7*	0.00032	0.0002	-0.05	0.09	-0.08	**0.0000**	**0.89**	0.2916	0.14	**0.0006**	**0.82**
R: A20, Uncus, Hipp (EC, SUB, CA)	L+R: A25., L: A11	7.8*	0.00069	0.0004	-0.12	0.04	-0.05	**0.0000**	**0.91**	0.0462	0.42	**0.0116**	**0.55**
R: A27, Hipp (FD, CA)	R: A11, A10	6.9	0.00152	0.0014	-0.04	0.06	-0.06	**0.0056**	**0.64**	0.2870	0.14	**0.0000**	**0.81**
R: Caudate, Hipp (CA, FD)	R: A9, A10	6.8	0.00163	0.0014	-0.08	0.07	-0.06	**0.0016**	**0.75**	0.3180	0.11	**0.0006**	**0.77**
R: Hipp (CA, SUB, FD)	R: A11, A10	6.6	0.00204	0.0016	-0.05	0.05	-0.06	**0.0034**	**0.67**	0.3732	0.08	**0.0004**	**0.82**
R: Uncus, A28, A34, Hipp (EC)	R: A44, A45	6.5	0.00228	0.0036	-0.06	0.08	0.11	**0.0024**	**0.70**	**0.0006**	**0.85**	0.2704	0.14
R: A35, A36, Hipp (SUB, CA)	R: A11	5.4	0.00611	0.0088	-0.09	0.04	-0.04	**0.0012**	**0.77**	0.1060	0.31	**0.0278**	**0.46**
R: Uncus, A34, Amyg, Hipp (EC)	R: A11	4.7	0.01134	0.0102	-0.01	0.06	-0.06	**0.0270**	**0.45**	0.1468	0.26	**0.0016**	**0.70**
ROI pair hypo-connectivity MCI vs CN													
R: A30, Hipp (FD, CA)	L: SMA	7.0	0.00145	0.0010	0.12	-0.01	0.14	**0.0020**	**0.73**	0.3148	0.11	**0.0016**	**0.75**
R: Uncus, A28, A35, Hipp (EC)	L+R: A10	6.4	0.00232	0.0012	0.14	0.03	-0.03	**0.0088**	**0.57**	**0.0002**	0.81	0.0930	0.32
R: Amyg, Hipp (CA)	R: A38, A21	5.9	0.00386	0.0052	0.15	0.04	0.17	**0.0030**	**0.63**	0.3686	0.08	**0.0010**	**0.78**
R: Hipp (CA, FD, SUB)	L+R: A11	5.8	0.00405	0.0048	0.02	-0.10	0.02	**0.0012**	**0.70**	0.4836	0.01	**0.0016**	**0.69**

ACC = anterior cingulate cortex; AD = Alzheimer's disease; Amyg = amygdala; CA = cornu ammonis; CN = cognitively normal; EC = entorhinal cortex; FD = dentate gyrus; FDR = false detection rate; Hipp = hippocampus; MCI = mild cognitive impairment; MTL = medial temporal lobe; ROI = region of interest; SMA = supplemental motor area; SUB = subiculum; *(Significant at FDR q =

3.5. Parcellation of functional connectivity changes of left MTL in the group-level MCI-CN contrast

The positions of left MTL anchor ROI masks for significant ROI pairs of interest in the MCI-CN contrast are shown in sagittal section (Figure 1 (top)) and coronal section (Figure 3 (left)). Positions of the corresponding non-anchor paired ROIs are discussed next and shown in Supplemental Figure 6. The spatial organization of the ten MTL anchor ROI masks was analyzed using AFNI *3dclust* which identified three clusters oriented along a ventral-medial to

[5] Supplemental Information Table 6 (Worksheet MCI-CN_Detail) provides additional details, including ROI MNI coordinates.

346 dorsal-lateral axis in the left MTL. First, in the ventral medial cluster, in the area of the
347 hippocampal head, the most medial anchor ROIs were positioned in the parahippocampal gyrus
348 (uncus), and Areas 35 and 36, and were ipsilaterally hyperconnected with a more rostral non-
349 anchor ROI positioned in Area 34. More laterally in this cluster, anchor ROI positions
350 progressively shifted to Area 28, hippocampus (subiculum and CA) and parahippocampal gyrus.
351 Functional connectivity changes with paired non-anchor ROIs consisted of hyperconnectivity
352 with ROIs in ipsilateral and contralateral Area 38, and hypoconnectivity with a contralateral ROI
353 positioned laterally in Area 45 and 47.

354 A second cluster of MTL anchor ROI masks, lateral and dorsal to the ventral medial cluster, was
355 positioned in its medial subregion in the hippocampus (subiculum, CA), and in its lateral
356 subregion in the hippocampus (CA) in the region of the caudate tail and parahippocampal gyrus.
357 The anchor ROI in this cluster was hyperconnected with its paired non-anchor ROI positioned in
358 contralateral lateral Area 10 adjacent to Area 47.

359 Last, in the dorsal cluster of anchor ROI masks, its medial subregion was positioned in Area 36
360 and hippocampus (CA, FD, subiculum), and in its lateral subregion in hippocampus (CA) in the
361 region of the caudate tail and parahippocampal gyrus. Functional connectivity changes in this
362 subzone included: a) an anchor ROI hyperconnected with a contralateral non-anchor ROI
363 positioned in lateral Area 10/11; b) an anchor ROI hypoconnected with a non-anchor ROI
364 located in precuneus; c) an anchor ROI hypoconnected with a non-anchor ROI located in anterior
365 cingulate cortex; and d) an anchor ROI simultaneously hyperconnected with a contralateral non-
366 anchor ROI located in the region of uncus, Area 28 and 36, and hypoconnected with a non-
367 anchor ROI located in precuneus.

368 In summary, in the left hemisphere, for the identified significant ROI pairs in the MCI-CN
369 contrast, the anchor MTL ROIs clustered within focal subregions of entorhinal and perirhinal
370 areas, hippocampus, and parahippocampal gyrus. The spatial pattern of functional connectivity
371 changes with corresponding non-anchor ROIs suggested that MTL subzones were: a) ventrally,
372 bilaterally hyperconnected, including uncus and Area 38; b) dorsally and laterally,
373 simultaneously hyperconnected and hypoconnected with distinct non-overlapping contralateral
374 lateral frontal cortical regions; and c) over an extended dorsal and lateral zone, hypoconnected
375 with midline regions associated with anterior and posterior default-mode network (DMN) nodes.

376 *3.6. Parcellation of functional connectivity changes of right MTL in the group-level MCI-CN*
377 *contrast*

378 The position of right MTL anchor ROI masks for significant ROI pairs of interest in the MCI-CN
379 contrast are shown in sagittal section (Figure 2 (top)) and coronal section (Figure 3 (left)).
380 Positions of the corresponding non-anchor paired ROIs are discussed next and shown in
381 Supplemental Figure 7. The spatial organization of the 13 MTL anchor ROI masks was analyzed
382 using AFNI *3dclust* which identified two clusters oriented along a ventral-medial to dorsal-
383 lateral axis. In the first cluster, near the head of the hippocampus, in its medial subregion,
384 anchor ROIs were positioned in the uncus, and Areas 28, 34, 35 and 36. Anchor ROI positions
385 in the middle and lateral subregions progressively shifted to the hippocampus (subiculum, FD
386 and CA). Pairwise functional connectivity with corresponding non-anchor ROIs consisted of an
387 interleaved pattern of hyperconnectivity and hypoconnectivity with small regions of overlap. In
388 the medial subregion, immediately adjacent anchor ROIs were either hyperconnected with an
389 ipsilateral lateral non-anchor ROI in Area 44 and 45, or hypoconnected bilaterally with a non-
390 anchor ROI in Area 10 at the midline. In the middle subregion there was a zone of

391 hypoconnectivity with an ipsilateral non-anchor ROI in the region of Area 38 and 21.
392 Immediately lateral to this hypoconnected anchor ROI, were a pair of anchor ROIs that were
393 hyperconnected with non-anchor ROIs positioned in contralateral uncus, Area 38 and 28. In the
394 most lateral subregion, anchor ROIs were hyperconnected bilaterally with a non-anchor ROI in
395 the region of Area 11 and 25 at the midline.

396 The second cluster of anchor ROIs, dorsal to the first, was characterized by multiple immediately
397 adjacent anchor ROIs with a distinct distribution of functional connectivity with corresponding
398 non-anchor ROIs. In its medial extent, anchor ROIs in this cluster were positioned in Area 35,
399 36 and hippocampus (CA, FD, subiculum) and in its lateral extent in hippocampus (CA, FD) in
400 the region of the caudate tail, but not parahippocampal gyrus. In the medial extent of this cluster
401 of anchor ROIs, functional connectivity changes with non-anchor ROIs consisted of
402 hyperconnectivity with an ipsilateral lateral ROI positioned in Area 10 and 11. In the lateral
403 extent of this cluster of anchor ROIs, there was hyperconnectivity with an ipsilateral lateral non-
404 anchor ROI whose position shifted to that of Area 9 and 10. In the medial subzone of this cluster
405 of anchor ROIs, there was functional hypoconnectivity with a corresponding paired non-anchor
406 ROI positioned in contralateral supplemental motor area (SMA) and in its lateral extent
407 hyperconnectivity bilaterally with a non-anchor ROI positioned in Area 11 at the midline.

408 In summary, in the right hemisphere in the transition from CN to MCI, the spatial pattern of
409 pairwise functional connectivity changes between anchor MTL and non-anchor ROIs suggests
410 that MTL subzones were: a) ventrally, hyperconnected with contralateral uncus and Area 38 and
411 hypoconnected with ipsilateral anterior Area 38; b) hyperconnected with ipsilateral lateral frontal
412 cortex; and c) hypoconnected with frontal cortical zones at the midline in regions adjacent to or
413 associated with anterior DMN midline nodes.

3.7. Significant pairwise ROI functional connectivity changes in the AD-CN group-level contrast

In the left hemisphere, an ROI pair was significant for functional connectivity changes in the AD-CN contrast for *post hoc* pairwise *t* test critical *p* value threshold less than the FDR-corrected, $p^*_{D,CN}$ = 0.0214, (q=0.05*, N=28 tests*). There were 21 significant AD-CN comparisons (Supplemental Tables 4 and 6). The MTL anchor ROI mask positions are shown in Figure 1 (bottom) and Figure 3 (right), and non-anchor ROI mask positions are shown in Supplemental Figure 8. Comprising the 21 significant comparisons were: a) nine hyperconnected pairs, Cohen's d, $0.52 \leq d \leq 0.86$, median=0.75; and b) 12 hypoconnected pairs, Cohen's d, $0.7 \leq d \leq 0.86$, median=0.64. There were more than twice as many AD-CN significant comparisons (N=21) as there were MCI-CN significant ROI comparisons (N=10). There were 1.5 times as many hyperconnected ROI pairs ($N_{AD\text{-}CN}$=9 vs $N_{MCI\text{-}CN}$=6) and 3.0 times as many hypoconnected ROI pairs ($N_{AD\text{-}CN}$=12 vs $N_{MCI\text{-}CN}$=4). Six of the nine significant hyperconnected and ten of the twelve significant hypoconnected ROI pairs were not significant in the MCI-CN contrast. Despite the increase in numbers of significant ROI pairs, the overall spatial organization of MTL ROI positions was similar to that of the MCI-CN contrast. The greater number of co-located anchor ROIs preferentially distributed in the ventral medial and dorsal lateral ROI clusters.

A striking feature in the AD-CN contrast was individual anchor MTL ROIs which formed multiple significant ROI pairs. Fourteen left hemisphere MTL ROIs comprised the anchor ROI in 21 significant ROI pairs. This was compared to nine MTL anchor ROIs that formed 10 significant ROI pairs in the MCI-CN contrast. In the AD-CN contrast, six MTL ROIs comprised the anchor element in two significant ROI pairs. The most common combination (four of six) was one hyperconnected pair and one hypoconnected pair. For example, an anchor ROI in

437 ventral MTL (Area 35) was hyperconnected with a non-anchor ROI located contralateral Area 38
438 and simultaneously hypoconnected with a non-anchor ROI in the region of the orbital gyrus at
439 the midline. As a second example, an anchor ROI in the dorsal MTL in hippocampus (CA) was
440 hyperconnected with a contralateral non-anchor ROI located in the region of uncus and
441 entorhinal cortex, and simultaneously hypoconnected with a non-anchor ROI in contralateral
442 lateral inferior temporal gyrus. In the single case of an anchor MTL ROI having two
443 hypoconnections, an anchor ROI positioned in hippocampus (CA) adjacent to the
444 parahippocampal gyrus, was hypoconnected with a non-anchor ROI located in precuneus at the
445 midline and hypoconnected with a non-anchor ROI located in the contralateral lateral frontal
446 cortex in Area 45 immediately adjacent to Area 47. Last, in the single case of an anchor MTL
447 ROI having two hyperconnections, an anchor ROI positioned in the region of Areas 28, 25, 36
448 and uncus, was *bilaterally* hyperconnected with a non-anchor ROI located in Area 38.

449 In the right hemisphere, ROI pairwise tests were significant for functional connectivity changes
450 in the AD-CN contrast with a *post hoc* pairwise *t* test critical *p* value threshold less than the
451 FDR-corrected, $p^*_{D,CN}$ = 0.0034, (q=0.05*, N=17 tests*). There were six significant comparisons
452 (Supplemental Tables 5 and 6). The MTL anchor ROI mask positions are shown in Figure 2
453 (bottom) and Figure 3 (right) and the paired non-anchor ROI mask positions are shown in
454 Supplemental Figure 9. Four of the six AD-CN comparisons were positive indicating
455 hyperconnectivity with Cohen's effect size d, $0.7 \leq d \leq 1.14$. Two of these four significant
456 comparisons were also significant in the MCI-CN contrast, indicating persistence of effect with
457 disease progression: hyperconnectivity with contralateral uncus; and hyperconnectivity with
458 ipsilateral Area 44 and 45. Two of these four significant comparisons were not significant in the
459 MCI-CN contrast with the following characteristics: a) both MTL anchor ROIs were positioned

in the region of the head of the hippocampus, entorhinal cortex and uncus; b) one (dorsal) was hyperconnected with a contralateral non-anchor ROI located in lateral Area 10; and c) the other (ventral) was hyperconnected with an ipsilateral non-anchor ROI located in medial Area 11 (nearly at the midline). Last, for two of the six significant AD-CN ROI pairs, neither of which was significant in the MCI-CN comparison, the pairwise functional connectivity change was hypoconnectivity (Cohen's d, $0.77 \leq d \leq 0.81$). The anchor ROIs in these pairs were positioned in the region of the head of the hippocampus, entorhinal cortex and uncus. One (dorsal) was hypoconnected with a non-anchor ROI located in Area 10 at the midline; the other (ventral) was hypoconnected with a non-anchor ROI located in ipsilateral lateral A10 adjacent to A46.

Summarizing left and right hemisphere jointly, the spatial pattern of functional connectivity changes from CN to D reflected a combination of consolidation, progression, and reversion of the changes observed in the CN to MCI contrast. First, there were not anchor ROIs positioned in additional MTL subzones. Second, additional significant ROIs in the AD-CN contrast clustered preferentially in the region of the head of the hippocampus, entorhinal cortex and uncus, compared to the wider distribution in the MCI-CN contrast. Third, significant AD-CN non-anchor ROIs were positioned within similar cortical regions (e.g., lateral frontal cortex, midline regions) as in the MCI-CN contrast or in additional regions (e.g., right inferior temporal cortex). Last, a combination of reversion and consolidation was evident in the absence in right hemisphere in the AD-CN contrast of the more dorsal cluster of ROIs present in MCI-CN contrast.

480 *3.8. MCI-CN functional connectivity changes may persist or revert in the group-level AD-CN*
481 *contrast*

482 In the AD-CN contrast there were functional connectivity changes that persisted or were
483 transient compared to the MCI-CN contrast. In the left hemisphere for three of six MCI-CN
484 hyperconnected ROI pairs and for two of four MCI-CN hypoconnected ROI pairs, the functional
485 connectivity change persisted or was amplified in the AD-CN contrast. In the right hemisphere,
486 however, only two of nine MCI-CN hyperconnected ROI pairs and for one of four MCI-CN
487 hypoconnected ROI pairs, did the functional connectivity change persist. Examples of persistent
488 effects included: a) left MTL and its ipsilateral and contralateral hyperconnectivity with Area 38;
489 b) left MTL hypoconnectivity bilaterally with anterior cingulate cortex and precuneus; and c)
490 right MTL hypoconnectivity bilaterally with Area 10 at the midline. Of the set of ROI pairs with
491 persistent functional connectivity changes in the MCI-CN and AD-CN contrasts, only one ROI
492 pair was monotone, i.e., significant in all three contrasts MCI-CN, AD-CN, and AD-MCI. For
493 this progressively hyperconnected ROI pair, the MTL ROI element was positioned in left MTL
494 in the region of Areas 28, 35, 36 and uncus, and the second element was in a contralateral region
495 with focal point in Area 38. In contrast, for three of six hyperconnected and for two of four
496 hypoconnected significant MCI-CN ROI pairs in the left hemisphere, and in all but three of 13
497 significant ROI pairs in the right hemisphere, the changes reversed course such that there was no
498 significant difference in the AD-CN contrast.

499 In summary, there were monotonic and non-monotonic, transient and persistent changes in
500 functional connectivity between the identified ROI pairs in the AD-CN contrast compared with
501 the MCI-CN contrast. The enduring changes observed across the CN, MCI and D progression
502 include mutual bilateral hyperconnectivity between MTL and Area 38, and hypoconnectivity of

503 left and right MTL with anterior and posterior regions immediately adjacent to or associated with
504 midline DMN nodes.

505 *3.9. Sensitivity analysis*

506 In preliminary studies, we assessed by spot-checking the sensitivity of the detection of
507 statistically significant (one-way, three-factor ANOVA ROI pair) functional connectivity
508 comparisons to changes in preprocessing parameters. The results reported in this study were
509 obtained with FWHM = 4.0 mm spatial smoothing in the AFNI preprocessing stage. Smoothing
510 with FWHM = 6.0 mm or FWHM = 8.0 mm and FDR $q = 0.05$, eliminated the observation of
511 significant ANOVA trials. In such cases, we did not proceed to the 5000 permutation repeated
512 measures test (although we observed anecdotally using a 1000 permutation repeated measures
513 test that a few significant tests were observed). Similarly, present results were obtained using an
514 ROI defined as the 6.0 mm radius volume centered at a given source or target ROI seed.
515 Expansion to an 8.0 mm radius volume eliminated the observation of significant ANOVA tests.
516 In any of the above tests, when we relaxed the FDR q value, for example, to $0.05 \leq q \leq 0.20$,
517 progressively greater numbers of significant ANOVA tests were observed. These preliminary
518 observations drove the decision to proceed with FWHM = 4.0 mm and ROI volume radius = 6.0
519 mm where, with a conservative FDR $q = 0.05$.

520 We assessed the reproducibility of the reported results under repeated measures with different
521 random number generator seeds in the 5000-trial permuted repeated measures. We completed
522 two additional 5000-trial runs for the left hemisphere data and found that for the MCI-CN
523 contrast (the only contrast analyzed in detail) there were comparable numbers of significant tests

and same, adjacent or overlapping ROI pairs with comparable F statistic values to those reported here. The remaining pairs were typically in positions adjacent to or overlapped those reported.

We determined the impact of an even more conservative FDR value q = 0.01 on the reported pairwise ROI functional connectivity results. For the left hemisphere, the FDR corrected F statistic p value was ($p_F^* < 0.0018$) and there remained nine significant ANOVA tests. For the significant ANOVA tests only, *post hoc* pairwise t tests were computed and FDR-corrected (q = 0.01, N =9 tests) independently per contrast: $p_{MCI,CN}^*$ = <0.0001; $p_{D,CN}^*$ = 0.0052; $p_{D,MCI}^*$ = 0.0014. There were no significant hypoconnected ROI pairs. There were two significant hyperconnected MCI-CN pairs and these are shown in Table 3 marked with an asterisk. For the right hemisphere, the FDR corrected F statistic p value was ($p_F^* < 0.0006$) and there remained five significant ANOVA tests. For the significant ANOVA tests only, *post hoc* pairwise t tests were computed and FDR-corrected (q = 0.01, N =5 tests) independently per contrast: $p_{MCI,CN}^*$ = <0.0001; $p_{D,CN}^*$ = 0.0018; $p_{D,MCI}^*$ = 0.0008. There were no significant hypoconnected ROI pairs. There were three significant hyperconnected MCI-CN pairs and these are shown in Table 4 marked with an asterisk. In summary, the impact of an even more conservative FDR value q = 0.01 on reported MCI-CN significant comparisons is that the findings of hypoconnected ROI pairs are not conserved; the findings of hyperconnected ROI pairs are conserved. For the D-CN contrast, findings are confirmed, although with reduced numbers, in that there remain significant comparisons in left and right hemisphere representing hyperconnected ROI pairs and hypoconnected ROI pairs.

545 # 4. Discussion

546 We report evidence that disruption of task-free resting state network functional connectivity is
547 present before the Alzheimer's Disease pathophysiological stage at which neurodegeneration has
548 sufficiently progressed to be detected. The results were obtained by comparing resting-state
549 fMRI connectivity with an automated analysis of standard (1mm) structural T1 MRI as cortical
550 thinning, subcortical structural volume reduction and hippocampal subfield volume reduction.
551 An anatomically bootstrapped, data-driven procedure identified statistically significant
552 comparisons in resting state functional networks having edges where one node was in the MTL
553 and the other was at anatomical locations corresponding with DMN nodes. Further, we observed
554 a diversity of effects of Alzheimer's Disease progression on ROI pairwise functional
555 connectivity, including complex patterns of hypoconnectivity *and* hyperconnectivity across the
556 MCI-CN and AD-CN transitions confirming that the effect of Alzheimer's Disease progression
557 on functional connectivity is more complex than simply there being monotonic loss or gain of
558 functional connectivity.

559 ## *4.1. Structural imaging findings provide an important control for functional connectivity*
560 *findings*

561 A key structural MRI finding in Alzheimer's Disease is cortical atrophy (thinning and volume
562 loss) that correlates with symptom severity and has a demonstrated diagnostic and prognostic
563 value (Braak and Braak, 1991; Fan, et al., 2008; Davatizikos, et al., 2009; Lerch, 2005; Jack, et
564 al., 2008; Dickerson, et al., 2009; Misra, et al., 2009; Miller-Thomas, et al., 2016). This finding
565 was reproduced here (Supplemental Table 1) and served as an important control for functional
566 connectivity analysis. We hypothesized that the anatomical locations of the cortical ROIs

567 observed in our functional connectivity analysis would correspond with previously demonstrated
568 spatial patterns of cortical thinning. Indeed, the anatomically boot-strapped data-driven method
569 employed in the present study identified significant MCI-CN cortical ROI anatomical positions
570 in areas known to be most vulnerable to cortical thinning. These included the rostral medial
571 temporal cortex, temporal pole and superior frontal regions, but not the inferior temporal cortex.
572 Significant functional connectivity changes involving inferior temporal cortex were however
573 observed in the AD-CN contrast. The absence of statistically significant cortical thinning in the
574 MCI-CN contrast suggests that the observed functional connectivity changes may not solely be
575 accounted for as a reflection in MTL of mechanisms arising in cortical regions.

576 The present study also reproduces key findings of hippocampal volume and hippocampal
577 subfield volume loss with Alzheimer's Disease progression (Hyman, et al., 1984; Braak and
578 Braak, 1991; Jack, et al., 1992, 1998; Schuff, et al., 2009; Boutet, et al., 2014; Sorensen, et al.,
579 2016; Wolk, et al., 2017). The confirmation of expected significant volume loss and significant
580 functional connectivity changes in the AD-CN contrast provides a control for the present MCI-
581 CN and AD-CN findings.

582 The absence of significant reduction in whole hippocampus volume and hippocampal subfield
583 volumes in the MCI-CN contrast reported above is with respect to a widely available benchmark:
584 up-to-date automated analysis (FreeSurfer) of research quality T1-weighted scans (1.0 x 1.0 x 1.0
585 mm^3). We do not conclude that there are no morphometric changes taking place
586 contemporaneously with the CN to MCI transition. Wolk, et al. (2017), analyzed high resolution
587 (~0.4 x 0.4 x 2 mm^3) T2-weighted MRI scans orthogonal to the long axis of the hippocampus at
588 autopsy. They reported significant group-level reduction of MTL subfield volumes (e.g., Area
589 35, perirhinal cortex) in the CN to early MCI transition where whole hippocampus volumes were

590 not significantly different. In a feasibility study of an *in vivo* approach, Boutet, et al., (2017)
591 used 7T MRI to detect hippocampal subfield volume changes in an AD–CN contrast. These
592 studies, together with present results, indicate the potential of dual functional and high-resolution
593 morphometric biomarkers for detecting the earliest stages in the Alzheimer's Disease
594 pathophysiology.

595 *4.2. Comparison to prior work*

596 With respect to our functional connectivity findings, five published reports are of particular
597 relevance (Grecius, et al., 2004; Jones, et al, 2011; Brier, et al., 2012; Ward, et al., 2014; Dillen,
598 et al., 2017). Grecius, et al., (2004) performed a pairwise group-level (healthy control (N=14) vs
599 very mild or mild Alzheimer's Disease (N=13)) independent components analysis (ICA) and
600 ROI analyses of steady-state DMN connectivity during a simple sensorimotor task in a cohort
601 drawn from the Washington University Alzheimer's Disease Research Center. Key findings
602 were: a) prominent bilateral coactivation of the hippocampus with DMN in both clinical groups;
603 and b) disruption of hippocampal – PCC connectivity in the Alzheimer's Disease group. Dillen
604 et al., (2017) performed a within-group and between-group analysis of hippocampus and DMN
605 node functional connectivity analysis in a cohort drawn from an outpatient population at the
606 Memory Clinic Cologne Julich (healthy control (N=25), subjective cognitive decline (SCD)
607 (N=28); and prodromal Alzheimer's Disease (N=25)). Significantly, they reported a decoupling
608 of hippocampus with posterior cortical DMN nodes in both SCD and prodromal Alzheimer's
609 Disease groups.

610 Brier, et al., (2012) performed a cross-sectional analysis of five task-free resting state networks
611 (RSN), including DMN, in a cohort drawn from the Knight Alzheimer's Disease Research

612 Center at Washington University in St. Louis. Subjects were assigned to one of three groups
613 according to CDR scores 0 (cognitively normal, N=386), 0.5 (very mild AD, N=91), and 1.0
614 (mild AD, N=33). The study reported summary measures of intranetwork and internetwork
615 steady-state correlation structure based on Fisher z-transformed pairwise Pearson correlation
616 analysis of ROI seed-based average time series. While not uniformly statistically significant, the
617 conclusion was that there was group-level progressive loss of intranetwork and internetwork
618 connectivity. The study also reported results of the effect of clinical group (CN, MCI,
619 Alzheimer's Disease) on ROI pair-wise functional connectivity between PCC and eight other
620 DMN nodes. For two ROI pairs (PCC – medial prefrontal cortex; PCC –left inferior temporal
621 lobe) there was a statistically significant reduction of connectivity in the CDR 0.5 group
622 compared to the CDR 0 group. Present results confirm the Brier, et al. observation of ROI pair-
623 wise functional connectivity loss in the MCI-CN comparison. They also extend the Brier, et al.
624 results. First, where Brier, et al., utilized a single ROI seed to estimate midline DMN structures
625 (e.g., PCC, thalamus), the present study utilized an anatomically bootstrapped data-driven
626 method that identified distinct left and right ROI seeds in these structures. The result was a more
627 fine-grained ROI pair-wise analysis which led to the observation of widespread left- and right-
628 hemispheric MTL hyperconnectivity ventrally together with disconnection with midline DMN
629 and DMN coactivated regions. Second, by design, the present study included hippocampus and
630 other MTL structures in the analysis and presented evidence that these structures are involved in
631 the loss of functional connectivity in the MCI-CN comparison.

632 Jones, et al. (2011) performed group-level functional connectivity analyses of task-free steady-
633 state DMN connectivity in cohorts drawn from the Mayo Clinic Alzheimer's Disease Research
634 Center and Mayo Clinic Study of Aging. Age-related changes in DMN functional connectivity

635 were analyzed using an ICA approach in a cognitively normal cohort (N=341). The age-related
636 changes consisted of differential effects in anterior and posterior DMN connectivity: a) anterior
637 DMN showed both increases and decreases in connectivity within the frontal lobe; and b)
638 posterior DMN showed a pattern of predominantly but not exclusively decreases in connectivity.
639 An age-matched CN and Alzheimer's Disease group analysis using both ICA and seed-based
640 ROI approaches concluded that DMN connectivity changes in Alzheimer's Disease represent an
641 acceleration of the same aging pattern observed in the control sample. The present study
642 complements these findings by providing additional detailed parcellation of changes in MTL,
643 separately analyzed in left and right hemisphere.

644 Ward, et al., (2014), in their study comparing resting state data and an associative memory
645 encoding task, concluded that the parahippocampal gyrus is the primary hub of the DMN in the
646 MTL during resting state. Their report ends with the suggestion that measuring PHG
647 connectivity may provide a biomarker of early Alzheimer's Disease. The present study,
648 although motivated by a different hypothesis (that functional connectivity changes temporally
649 precede detection of significant neurodegeneration) and using an entirely independent analysis
650 method (anatomically bootstrapped, data-driven method), provides quantitative evidence in
651 support of the Ward, et al., suggestion. We observe evidence of functional disconnection
652 bilaterally between posterior cortical DMN nodes (anterior cingulate cortex, precuneous) and
653 parahippocampal gyrus as part of a larger pattern of disruption involving anterior and posterior
654 DMN, and subcortical structures including hippocampus and parahippocampal gyrus.

655 *4.3. Limitations*

656 Limitations of the present study relate to the study population, the imaging data and
657 preprocessing methods. First, by excluding participants with other neurological injury or
658 findings, the study population was not representative of a general age-matched clinical
659 population. Second, the effect of the "penciling artefact", found in ADNI image data in left
660 lateral frontal cortex, on functional connectivity measures is unknown and introduces uncertainty
661 in the interpretation of present results. For example, there was a multiplicity of significant ROI
662 pairs between right MTL and ipsilateral lateral frontal cortex. There was not a comparable
663 finding in the left hemisphere, whereas there were bilateral findings with respect to midline
664 ROIs. Third, the present study applied in the pre-processing stage an atlas (AFNI: MNIavg152)
665 derived from younger brains than used in this study which could inject systematic error into the
666 data. Similarly, the FreeSurfer parameters were the default set which may be sub-optimal given
667 the population comprising this study. Last, there is not a consensus regarding the use or non-use
668 of GSR (Murphy and Fox, 2017) and the present study did not apply GSR. The reasoning was
669 two-fold. First, given the "penciling artefact" in ADNI data, it was problematic whether and
670 how to obtain a viable global signal estimate. Second, the preprocessing procedure estimated
671 and removed motion confounds and the ROI identification procedure applied ventricle and white
672 matter masks to minimize the influence of non-grey matter signals. However, any global or
673 large-scale regional neuronal fluctuations would not be controlled in this procedure.

674 *4.4. Translational considerations*

675 A challenge in the consideration of functional connectivity biomarkers is that there are in clinical
676 use well-established semi-quantitative structural biomarkers of Alzheimer's Disease (Fazekas, et

677 al., 1987; Scheltens, et al., 1992; Wahlund, et al., 2001). These methods have been extended in
678 clinical practice and medical research to include T1-based quantitative semi-automated and
679 automated methods for mild cognitive impairment and Alzheimer's Disease diagnosis, tracking
680 and prognosis (Dale, et al., 1999; Chupin, et al., 2009; Davatzikos, et al., 2009; Leung, et al.,
681 2010; Leung, et al., 2013; Misra, et al., 2016; Schuff, et al., 2009; Sorensen, et al, 2016).

682 The development of semi-automatic and automatic derivation of resting-state functional
683 connectivity biomarkers for Alzheimer's Disease classification is comparatively new (Grecius, et
684 al., 2004; Sepulcre, et al., 2017; and Wiepert, et al., 2017). First, Grecius, et al., (2004) applied a
685 goodness-of-fit test between an ICA-derived PCC-based or whole DMN-based templates and
686 individual subject images to classify Alzheimer's Disease or healthy ageing individuals. Second,
687 Wiepert, et al., (2017), proposed a network failure quotient (NFQ). The measure combined the
688 increases and decreases in DMN subsystem connectivity with Alzheimer's Disease progression
689 into a single statistic. The authors demonstrated that the statistic ("trained" in an ADNI cohort)
690 had the greatest effect size in differentiating CN and AD in a distinct cohort (Mayo Clinic).
691 Last, Sepulcre, et al., (2017) applied graph theory methods to demonstrate distinct associations
692 between functional connectivity changes in cognitively normal aging brains and cortical patterns
693 of *in vivo* tau and amyloid β positron emission tomography imaging. A remaining challenge is
694 to fully characterize classification sensitivity and specificity of functional connectivity
695 biomarkers compared to CSF-derived, plasma-derived and *in vivo* and structural imagine
696 modalities.

697 *4.5. Conclusion*

698 The contribution of the present study in the context of established structural and emerging
699 resting-state functional connectivity biomarkers is four-fold. First, we demonstrated that
700 functional connectivity changes were detected where structural changes were not yet in evidence
701 using widely available imaging clinic resources. Second, we measured functional connectivity
702 changes anchored in the MTL structures directly implicated in the earliest stages of Alzheimer's
703 Disease. Third, we observed a complex pattern of changes: monotonic and non-monotonic, and
704 persistent and reverting patterns of hyperconnectivity and hypoconnectivity, in a spatial
705 organization closely related to the default-mode network. Last, we adopted a multi-modal
706 functional-structural approach and demonstrated differential potential clinical value of resting-
707 state functional connectivity biomarkers in Alzheimer's Disease diagnosis, tracking and
708 prognosis.

709 # 5. Acknowledgements

710 Data collection and sharing for this project was funded by the Alzheimer's Disease Neuroimaging
711 Initiative (ADNI) (National Institutes of Health Grant U01 AG024904) and DOD ADNI (Department of
712 Defense award number W81XWH-12-2-0012). ADNI is funded by the National Institute on Aging, the
713 National Institute of Biomedical Imaging and Bioengineering, and through generous contributions from
714 the following: AbbVie, Alzheimer's Association; Alzheimer's Drug Discovery Foundation; Araclon
715 Biotech; BioClinica, Inc.; Biogen; Bristol-Myers Squibb Company; CereSpir, Inc.; Cogstate; Eisai Inc.;
716 Elan Pharmaceuticals, Inc.; Eli Lilly and Company; EuroImmun; F. Hoffmann-La Roche Ltd and its
717 affiliated company Genentech, Inc.; Fujirebio; GE Healthcare; IXICO Ltd.; Janssen Alzheimer
718 Immunotherapy Research & Development, LLC.; Johnson & Johnson Pharmaceutical Research &
719 Development LLC; Lumosity; Lundbeck; Merck & Co., Inc.; Meso Scale Diagnostics, LLC.; NeuroRx
720 Research; Neurotrack Technologies; Novartis Pharmaceuticals Corporation; Pfizer Inc.; Piramal Imaging;
721 Servier; Takeda Pharmaceutical Company; and Transition Therapeutics. The Canadian Institutes of
722 Health Research is providing funds to support ADNI clinical sites in Canada. Private sector contributions
723 are facilitated by the Foundation for the National Institutes of Health (www.fnih.org). The grantee
724 organization is the Northern California Institute for Research and Education, and the study is coordinated
725 by the Alzheimer's Therapeutic Research Institute at the University of Southern California. ADNI data
726 are disseminated by the Laboratory for Neuro Imaging at the University of Southern California.

727

728 # 6. References

729 Albert, M. S. (2011). The diagnosis of mild cognitive impairment due to Alzheimer's
730 Disease: Recommendations from the National Institute on Aging-Alzheimer's Association
731 workgroups on diagnostic guidelines for Alzheimer's Disease. *Alzheimer's & Dementia.* **7**,
732 270-279.

733 Benjamini, Y. and Hochberg, Y. (1995). Controlling the false discovery rate: A practical
734 and powerful approach to multiple testing. *J. Roy. Statist. Soc. Ser. B* **57**, 289-300.

735 Boutet, C., Chupin, M., Lehericy, S., et al. (2014). Detection of volume loss in hippocampal
736 layers in Alzheimer's Disease using 7T MRI: A feasibility study. *Neuroimage: Clinical.* **5**,
737 341-348.

738 Braak, H., Braak, E. (1985). On areas of transition between entorhinal allocortex and
739 temporal isocortex in the human brain: normal morphology and lamina-specific pathology in
740 Alzheimer's Disease. *Acta Neuropathol*. **68**, 325–332.

741 Braak, H., Braak, E. (1991). Neuropathological stageing of Alzhiemer-related changes. *Acta*
742 *Neuropathol.* **82**, 239–259.

743 Brier, M. R., Thomas, J.B., Snyder, A. Z., et al. (2012). Loss of intranetwork and
744 internetwork resting state functional connections with Alzheimer's Disease progression. *J*
745 *Neurosci.* **32**, 8890-8899.

746 Buckner, R. L., Snyder, A. Z., Shannon, B. J., et al. (2005). Molecular, structural, and
747 functional characterization of Alzheimer's Disease: evidence for a relationship between
748 default activity, amyloid, and memory. *J. Neurosci.* **25**, 7709-17.

749 Cai, S., Huang, L., Zou, J., et al. (2015). Changes in thalamic connectivity in the early and
750 late stages of amnestic mild cognitive impairment: a resting-state functional magnetic
751 resonance study from ADNI. *PLoS ONE* 10(2): e0115573.

752 Cox, R. W. (1996). AFNI: software for analysis and visualization of functional magnetic
753 resonance neuroimages. *Comp Biomed Res.* **29**, 1762-173.

754 Dale, A.M., Fischl, B., Sereno, M.I. (1999). Cortical surface-based analysis. I.
755 Segmentation and surface reconstruction. *Neuroimage* **9**, 179-194.

756 Davatzikos, C., Xu, F., An, Y., et al. (2009). Longitudinal progression of Alzheimer's-like
757 patterns of atrophy in normal older adults: the SPARE-D index. *Brain*. **132**, 2026-2036.

758 Chupin, M., Gerardin, E., Cuingnet, R., et al. (2009). Fully automatic hippocampus
759 segmentation and classification in Alzheimer's Disease and mild cognitive impairment
760 applied on data from ADNI. *Hippocampus*. **19**, 579-587.

761 Dickerson, B. C., Bakkour, A., Salat, D. H., et al. (2009). The cortical signature of
762 Alzheimer's Disease: Regionally specific cortical thinning relates to symptom severity in
763 very mild to mild D dementia and is detectable in asymptomatic amyloid-positive
764 individuals. *Cerebral Cortex.* **19**, 497-510.

765 Dillen, K. N. H., Jacobs, H. I. L., Kukolja, J., et al. (2017). Functional disintegration of the
766 default mode network in prodromal Alzheimer's Disease. *J. Alzheimer's Disease*. **59**:169–
767 187.

768 Efron, B. (2010). Large-scale inference: Empirical Bayes methods for estimation, testing
769 and prediction. IMS Monographs. Cambridge: Cambridge University Press.

770 Eklund, A., Nichols, T. E., and Knutsson, H. (2016). Cluster failure: Why fMRI inferences
771 for spatial extent have inflated false-positive rates. *Proc. Natl. Acad. Sci. USA.* **113**, 7900-
772 7905.

773 Fan, Y., Batmanghelich, N., Clark, C. M., et al. (2008). Spatial patterns of brain atrophy in
774 MCI patients, identified via high-dimensional pattern classification, predict subsequent
775 cognitive decline. *Neuroimage*. **39**, 1731-1743.

776 Fazekas, F., Chawluk, J. B., Alavi, A., et al. (1987). MR signal abnormalities at 1.5 T in
777 Alzheimer's dementia and normal aging. *Am J Roentgenol.* **149**, 351-6.

778 Greicius, M. D., Srivastava, G., Reiss, A. L., et al. (2004). Default-mode network activity
779 distinguishes Alzheimer's Disease from healthy aging: evidence from functional MRI. *Proc.*
780 *Natl. Acad. Sci. USA* **101**, 4637-4642.

781 Huijbers, W., Mormino, E. C., Schultz, A. P., et al. (2015). Amyloid-β deposition in mild
782 cognitive impairment is associated with increased hippocampal activity, atrophy and clinical
783 progression. *Brain*. **138**, 1023-1035.

784 Jack, C. R., Petersen, R. C., O'Brien, P. C., et al. (1992). MR-based hippocampal volumetry
785 in the diagnosis of Alzheimer's Disease. *Neurology*. **42**, 183-188.

786 Jack, C. R., Petersen, R. C., Xu, Y., et al. (1998). The rate of medial temporal lobe atrophy
787 in typical aging and Alzheimer's Disease. *Neurol*. **51**, 993-999.

788 Jack, C. R., Bernstein, M. A., Fox, N. C., et al. (2008). The Alzheimer's Disease
789 neuroimaging initiative (ADNI): MRI methods. *J. Magn. Reson Imaging.* **27**, 685–691.

790 Jack, C. R, Albert, M. S., Knopman, D. S., et al. (2011a). Introduction to the
791 recommendations from the National Institute on Aging-Alzheimer's Association workgroups
792 on diagnostic guidelines for Alzheimer's Disease. *Alzheimer's & Dementia.* **7**, 257-262.

793 Jack, C. R. (2011b). Alliance for aging research AD biomarkers group: structural MRI.
794 *Neurobiol. Aging*. **32**, S48-S57.

795 Jack, C. R., Knopman, D. S., Jagust, W. J., et al. (2013). Update on hypothetical model of
796 Alzheimer's Disease biomarkers. *Lancet Neurol.* **12**, 207-216.

797 Jack, C. R., Bennett, D. A., Blennow, K., et al. (2018). NIA-AA research framework:
798 Toward a biological definition of Alzheimer's Disease. *Alzheimer's & Dementia.* **14**, 535-
799 562.

800 Jones, D.T., Machulda, M. M., Vemuri, P., et al. (2011). Age-related changes in the default
801 mode network are more advanced in Alzheimer disease. *Neurology*. **77**, 1524-1531.

802 Jones, D.T., Vemuri, P., Murphy, M. C., et al. (2012). Non-stationarity in the resting brain's
803 modular architecture. *PLoS ONE* 7(6) e39731.

804 Jones, D. T., Knopman, D. S., Gunter, J. L., et al. (2016). Cascading network failure across
805 the Alzheimer's Disease spectrum. *Brain*. **139**, 547-562.

806 Lerch, J. P., Pruessner, J. C., Zijdenbos, A., et al. (2005). Focal decline of cortical thickness
807 in Alzheimer's Disease identified by computational neuroanatomy. *Cerebral Cortex.* **15**,
808 996-1001.

809 Leung, K. K., Barnes, J., Ridgway, G. R., et al. (2010). Automated cross-sectional and
810 longitudinal hippocampal volume measurement in mild cognitive impairment and
811 Alzheimer's Disease. *Neuroimage*. **51**, 1345-1359.

812 Leung, K. K., Bartlett, J. W., Barnes, J., et al. (2013). Cerebral atrophy in mild cognitive
813 impairment and Alzheimer disease. *Neurology*. **80**, 648-654.

814 McKhann, G. M., Knopman, D. S., Chertkow, J., et al. (2011). The diagnosis of dementia
815 due to Alzheimer's Disease: recommendations from the National Institute on Aging-
816 Alzheimer's Association workgroups on diagnostic guidelines for Alzheimer's Disease.
817 *Alzheimer's & Dementia.* **7**, 263-269.

818 Miller-Thomas, M. M., Sipe, A. L., Benzinger, T. L., et al. (2016). Multimodality review of
819 amyloid-related diseases of the central nervous system. *Radiographics*. **36**, 1147-1163.

820 Misra, C., Fan, Y., Davatzikos, C. (2009). Baseline and longitudinal patterns of brain
821 atrophy in MCI patients, and their use in prediction of short-term conversion to AD: results
822 from ADNI. *Neuroimage*. **44**, 1415-1422.

823 Murphy, K. and M. D. Fox. (2017). Towards a consensus regarding global signal regression
824 for resting state functional connectivity MRI. *Neuroimage*. **154**, 169-173.

825 Nichols, T. E. and Holmes, A. P. (2002). Nonparametric permutation tests for functional
826 neuroimaging: A primer with examples. *Human Brain Mapp.* **15**, 1-25.

827 Scheltens, M., Leys, D., Barkhof, F., et al. (1992). Atrophy of medial temporal lobes on
828 MRI in "probable" Alzheimer's Disease and normal ageing: diagnostic value and
829 neuropsychological correlates. *J. Neurol. Neurosurg. Psychiatry*.

830 Schuff, N., Woerner, N., Boreta, L., et al. (2009). MRI of hippocampal volume loss in early
831 Alzheimer's Disease in relation to ApoE genotype and biomarkers. *Brain*. **132**, 1067-1077.

832 Sepulcre, J., Sabuncu, M. R., Li, Q., et al. (2017). Tau and amyloid β proteins distinctively
833 associate to functional network changes in the aging brain. *Alzheimer's & Dementia.* **13**,
834 1261-1269.

835 Sheline, Y. I. and Raichle, M. E. (2013). Resting state functional connectivity in preclinical
836 Alzheimer's Disease. *Biol. Psychiatry.* **74**, 340-347.

837 Smith, S. M., Zhang, Y., Jenkinson, M., et al. (2002). Accurate, robust and automated
838 longitudinal and cross-sectional brain change analysis. *Neuroimage*. **17**, 479-489.

839 Sorensen, L., Igel, C., Liv Hansen, N., et al. (2016). Early detection of Alzheimer's Disease
840 using MRI hippocampal texture. *Hum. Brain Mapp.* 37, 1148-1161.

841 Sorg, C., Reidl, V., Muhlau, M., et al. (2007). Selective changes of resting-state networks in
842 individuals at risk for Alzheimer's Disease. *Proc. Natl. Acad. Sci. USA*. **104**, 18760-18765.

843 Sperling, R.A., Dickerson, B. ., Pihlajamaki, M., et al. (2010). Functional alterations in
844 memory networks in early Alzheimer's Disease. *Neuromolecular Med.* 12**,** 27-43.

845 Sperling, R. A., Aisen, P. S., Beckett, L. A., et al. (2011). Toward defining the preclinical
846 stages of Alzheimer's Disease: Recommendations from the National Institute on Aging-
847 Alzheimer's Association workgroups on diagnostic guidelines for Alzheimer's Disease.
848 *Alzheimer's & Dementia.* **7**, 280-292.

849 Wahlund, L. O., Barkhof, F., Fazekas, F., et al. (2001). A new rating scale for age-related
850 white matter changes applicable to MRI and CT. *Stroke*. **32**, 1318-1322.

851 Ward, A. M., Schultz, A. P., Huijbers, W., et al. (2014). The parahippocampal gyrus links
852 the default-mode cortical network with the medial temporal lobe memory system. Hum
853 Brain Mapp. **35**:1061–1073.

854 Weiner, M.W., Veitch, D. P., Aisen, P. S., et al. (2015). Impact of the Alzheimer's Disease
855 neuroimaging initiative, 2004 to 2014. *Alzheimer's Dement.* **11**, 865-884.

856 Wiepert, D. A., Lowe, V. J., Knopman, D. S., et al. (2017). A robust biomarker of large-
857 scale network failure in Alzheimer's Disease. *Alzheimer's Dement.: Diag., Assess. & Dis.*
858 *Monit.* **6**, 152-161.

859 Wolk, D. A., Das, S. R., Mueller, S. G., et al. (2017). Medial temporal lobe subregional
860 morphometry using high resolution MRI in Alzheimer's Disease. *Neurobiol. Aging*.
861 49:204-213.

862 Woo, C-W., Chang, L. J., Lindquist, Wager, T. D. (2017). Building better biomarkers: brain
863 models in translational neuroimaging. *Nat. Neurosci.* **20**, 365-376.

864 Zhou, J., Greicius, M. D., Gennatas, E. D., et al. (2010). Divergent network connectivity
865 changes in behavioral variant frontotemporal dementia and Alzheimer's Disease. *Brain*.
866 **133**, 1352-1367.

867 # 7. Figures

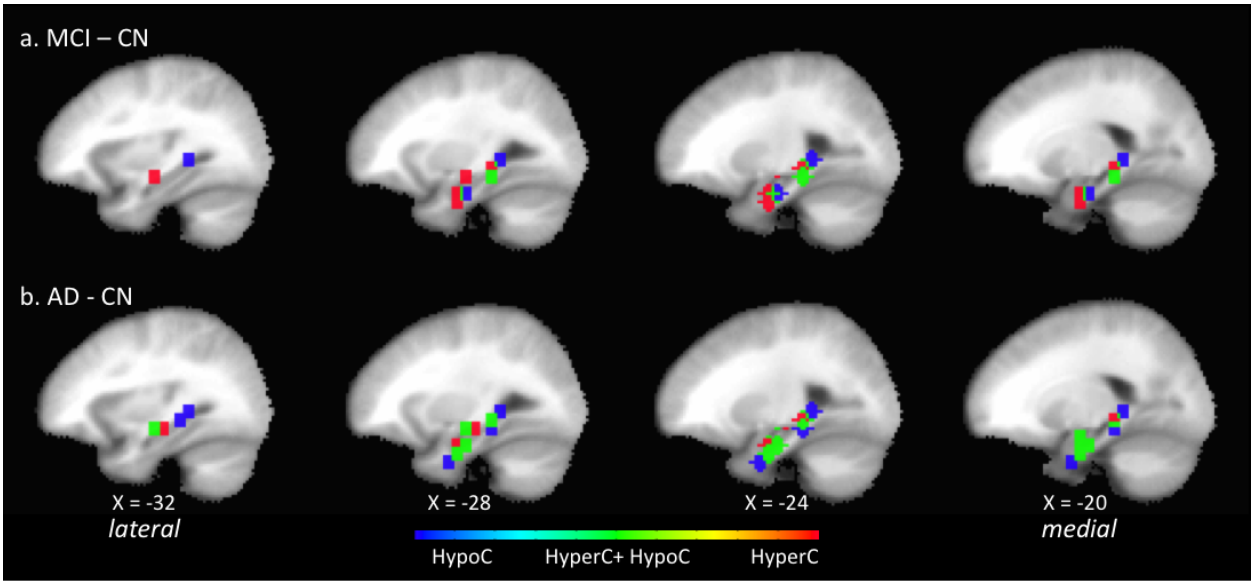

868

869 **Figure 1.** Position in the left hemisphere sagittal plane (4mm stride) of anchor MTL ROI
870 elements of significant ROI pairs of interest in the MCI – CN contrast (top) and D – CN contrast
871 (bottom). Shown are ROI masks for the 6-mm radius volume centered at the ROI seed. In both
872 contrasts, ROIs group in a ventral anterior subzone and a dorsal posterior subzone. There is
873 progressive change that may correlate with disease progression. In the D – CN contrast, there
874 are more significant ROI pairs of interest collectively whose anchor MTL ROIs cover a larger
875 extent of the MTL compared to MCI – CN. In addition, there is an increase in the number of
876 individual MTL ROIs that form multiple significant ROI pairs in which one pair is of type
877 hypoC and the other hyperC. Positions of the ROI paired with each MTL ROI shown are
878 summarized in Table 3, their MNI coordinates are listed in Supplemental Tables 4 and 6, and
879 corresponding image maps are shown Supplemental Figures 6 and 7. The direction of ROI pair
880 functional change is color-coded for hyperconnectivity (*red*), hypoconnectivity (*blue*), and
881 simultaneous hyperconnectivity and hypoconnectivity (*green*).

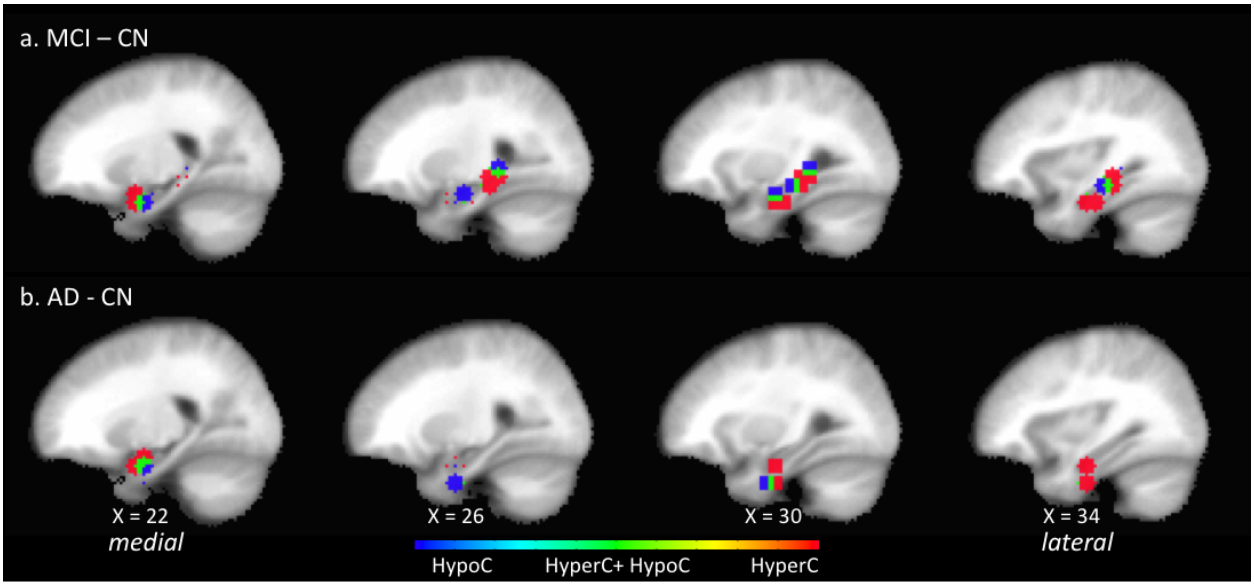

Figure 2. Position in the right hemisphere sagittal plane (4mm stride) of anchor MTL ROI elements of significant ROI pairs of interest in the MCI – CN contrast (top) and D – CN contrast (bottom). Shown are ROI masks for the 6-mm radius volume centered at the ROI seed. In the MCI - CN contrasts, but not the D – CN, ROIs group in a ventral anterior subzone and a dorsal posterior subzone. In the D – CN contrast, the dorsal posterior ROI cluster is not present, indicating that there may be a class of ROI pairwise functional connectivity changes that persist and those that are associated specifically with the CN to MCI transition. Positions of the ROI paired with each MTL ROI shown are summarized in Table 4, their MNI coordinates are listed in Supplemental Tables 5 and 6, and corresponding image maps are shown Supplemental Figures 8 and 9. The direction of ROI pair functional change is color-coded for hyperconnectivity (*red*), hypoconnectivity (*blue*), and simultaneous hyperconnectivity and hypoconnectivity (*green*).

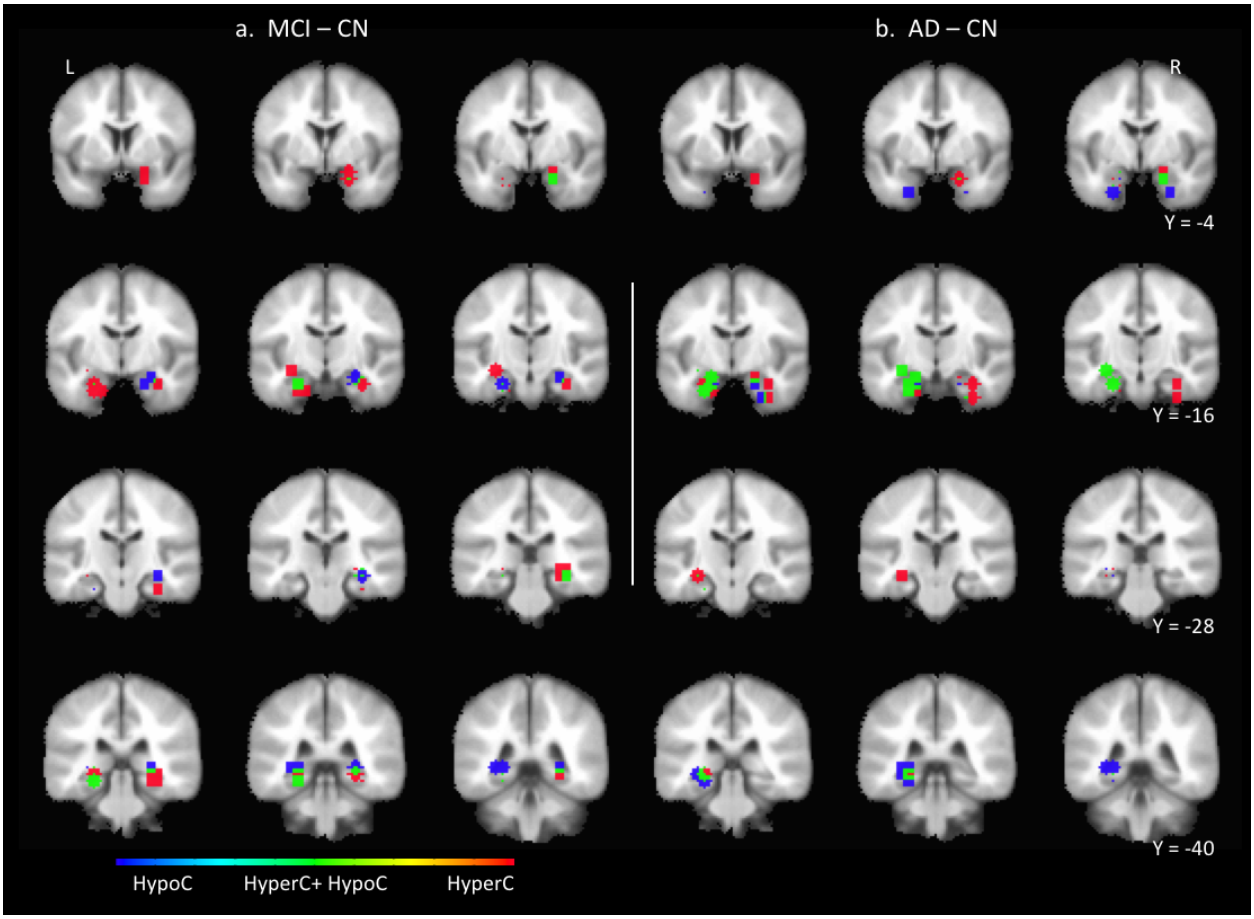

Figure 3. Coronal series showing the position of anchor MTL ROI elements of significant MCI – CN contrast ROI pairs (a) and D – CN contrast (b) ROI pairs. Shown are the anchor MTL ROI masks consisting of a 6-mm radius volume centered at the anchor MTL ROI seed. The direction of ROI pair functional change is color-coded for hyperconnectivity (*red*), hypoconnectivity (*blue*), and simultaneous hyperconnectivity and hypoconnectivity (*green*).

8. Supplemental Material - Tables

1. **Supplemental Information Table 1 (Cortical Thickness ANOVA Results).** Excel table containing the ANOVA F statistic and *p* value, *post hoc* pair-wise *t* statistic and *p* value, pair-wise Cohen's *d*, group average, and group average standard error, for 68 cortical region thickness estimates.

2. **Supplemental Information Table 2 (Subcortical Segmentation ANOVA Results).** Excel table containing the ANOVA F statistic and *p* value, *post hoc* pair-wise *t* statistic and *p* value, pair-wise Cohen's *d*, group average, and group average standard error, for 16 hippocampal subfield volume estimates.

3. **Supplemental Information Table 3 (Hippocampal Subfields ANOVA Results).** Excel table containing the ANOVA F statistic and *p* value, *post hoc* pair-wise *t* statistic and *p* value, pair-wise Cohen's *d*, group average, and group average standard error, for 22 subcortical structure volume estimates.

4. **Supplemental Information Table 4 (Left Hemisphere ANOVA Raw Results).** Excel tables containing left significant ROI pairs of interest, their ANOVA sample F statistic and *p* value, repeated measures permuted F statistic and *p* value, permutation estimated *post hoc* pair-wise *t* test *p* value, pair-wise Cohen's *d*, and group averages.

5. **Supplemental Information Table 5 (Right Hemisphere ANOVA Raw Results).** Excel tables containing right significant MCI-CN contrasts, their ANOVA sample F statistic and *p* value, repeated measures permuted F statistic and *p* value, permutation estimated *post hoc* pair-wise *t* test *p* value, pair-wise Cohen's *d*, and group averages.

6. **Supplemental Information Table 5 (Left and Right Tabulated ANOVA Results).** Excel tables containing right significant MCI-CN and AD-CN and AD-MCI contrasts, their ANOVA sample F statistic and *p* value, repeated measures permuted F statistic and *p* value, permutation estimated *post hoc* pair-wise *t* test *p* value, pair-wise Cohen's *d*, and

group averages, and including MNI coordinates. Tables correspond to Tables 3 and 4 in the main text.

938 # 9. Supplemental Material - Figures

939 1. **Supplemental Figure 1.** Resting-state fMRI processing block diagram.
940 2. **Supplemental Figure 2.** Spatial distribution in left (right) ROI masks sampled from
941 within the global left (right) MTL 3D "bounding box".
942 3. **Supplemental Figure 3.** Spatial distribution of ROI masks (each corresponding to the
943 center of mass of an F statistic cluster) identified by 3D ANOVA with a left MTL anchor
944 ROI.
945 4. **Supplemental Figure 4.** Spatial distribution of ROI masks (each corresponding to the
946 center of mass of an F statistic cluster) identified by 3D ANOVA with a right MTL
947 anchor ROI.
948 5. **Supplemental Figure 5.** Progression of cortical thinning in representative regions and
949 subcortical structure volume with clinical group. ANOVA results are shown in table
950 format in Supplemental Tables 1-3.
951 6. **Supplemental Figure 6. MCI-CN (left MTL anchors).** Spatial distribution of the non-
952 anchor ROI masks (where the anchor ROI mask was in left MTL) for the 10 significant
953 ROI pairwise comparisons in the MCI-CN contrast.
954 7. **Supplemental Figure 7. MCI-CN (right MTL anchors).** Spatial distribution of the
955 non-anchor ROI masks (where the anchor ROI mask was in right MTL) for the 10
956 significant ROI pairwise comparisons in the MCI-CN contrast.
957 8. **Supplemental Figure 8. AD-CN (left MTL anchors).** Spatial distribution of the non-
958 anchor ROI masks (where the anchor ROI mask was in left MTL) for the 21 significant
959 ROI pairwise comparisons in the AD-CN contrast.
960 9. **Supplemental Figure 9. AD-CN (right MTL anchors).** Spatial distribution of the non-
961 anchor ROI masks (where the anchor ROI mask was in right MTL) for the 6 significant
962 ROI pairwise comparisons in the AD-CN contrast.

Supplemental Figure 1. Grajski & Bressler. 2018.

Functional Connectivity Processing Stream

AD = Alzheimer's Disease; AFNI = Analysis of Functional Neuroimages; CN = Cognitively Normal; FDR = False Detection Rate; fMRI = functional Magnetic Resonance Imaging; MCI = Mild Cognitive Impairment; MNI = Montreal Neurological Institute; MTL = Medial Temporal Lobe; MRI = Magnetic Resonance Imaging; ROI = Region of Interest; rsfMRI = resting-state fMRI; SD = Standard Deviation; SUMA = Surface Mapping; V = Ventricles; WM = White Matter

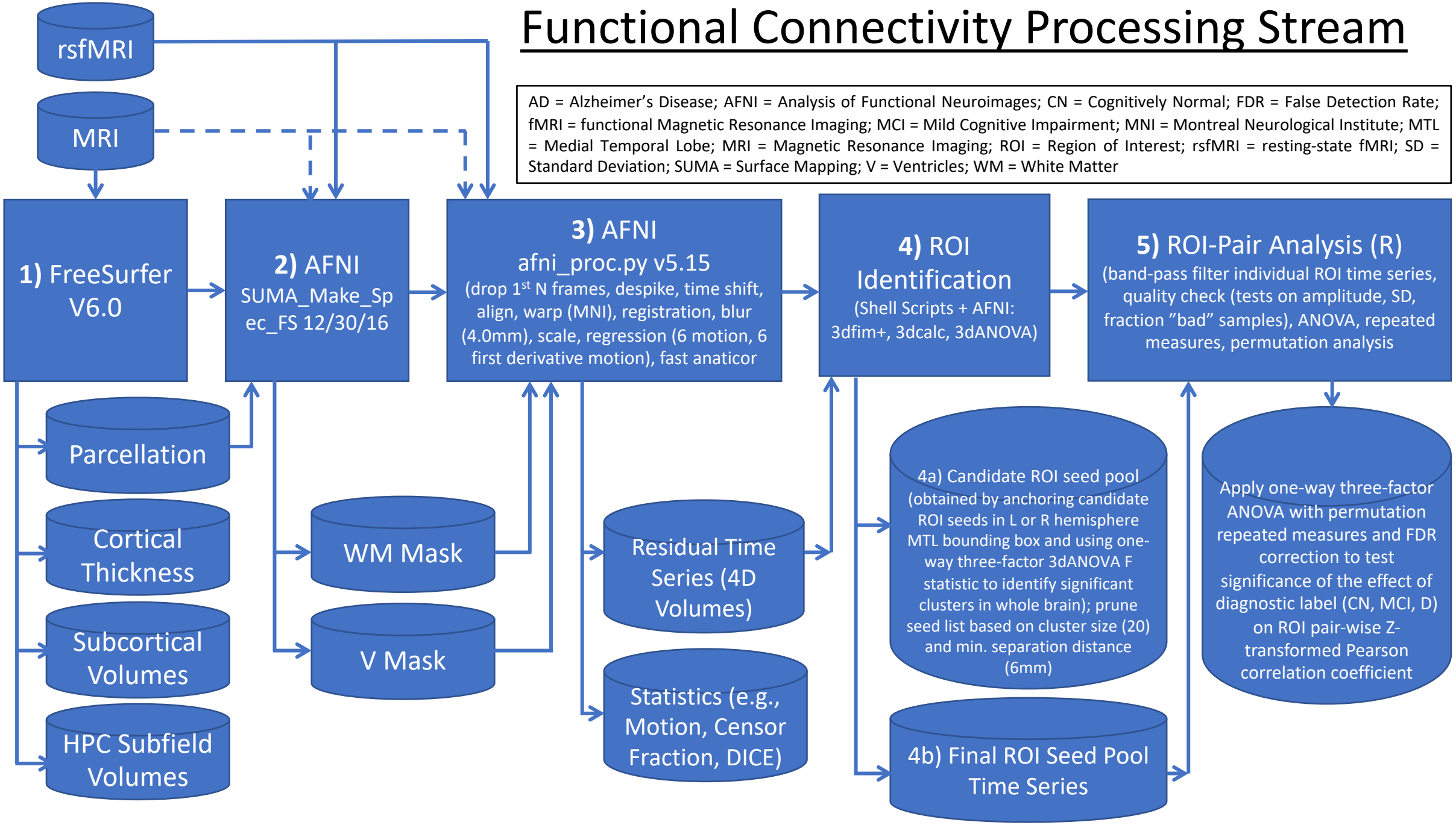

Supplemental Figure 2. Grajski & Bressler. 2018.

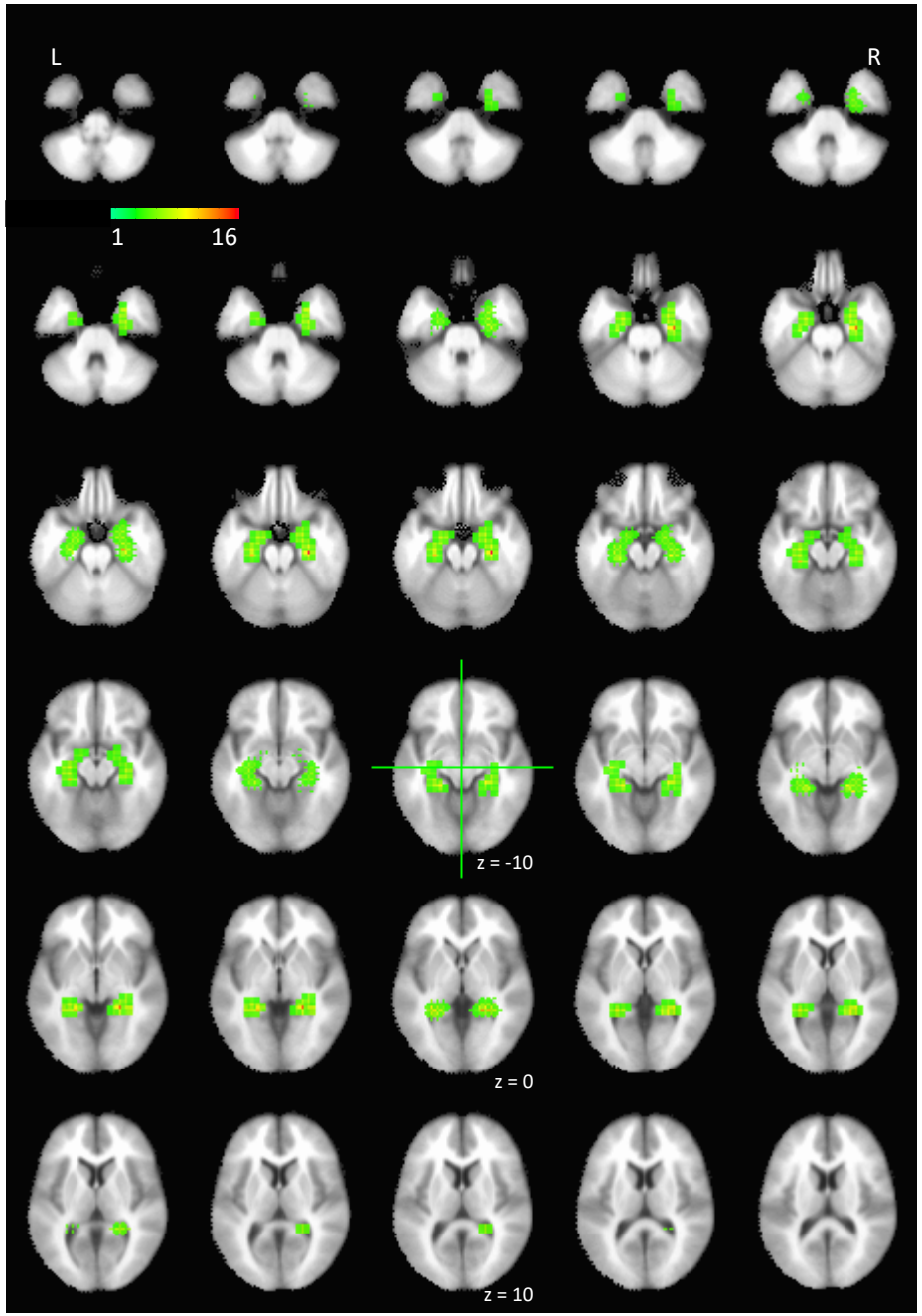

Spatial distribution in left (right) ROI masks sampled from within the global left (right) MTL 3D "bounding box".

Sum of MTL ROI masks (voxel values set to 0 (not included) or 1 (included)) used as the *starting point* for the MTL ROI identification procedure. At this processing stage, ROI masks overlap due to the 6mm sampling grid.

Crosshair MNI position: 0, -18, -10. Z-direction step size is 2mm.

Supplemental Figure 3.
Grajski & Bressler. 2018.

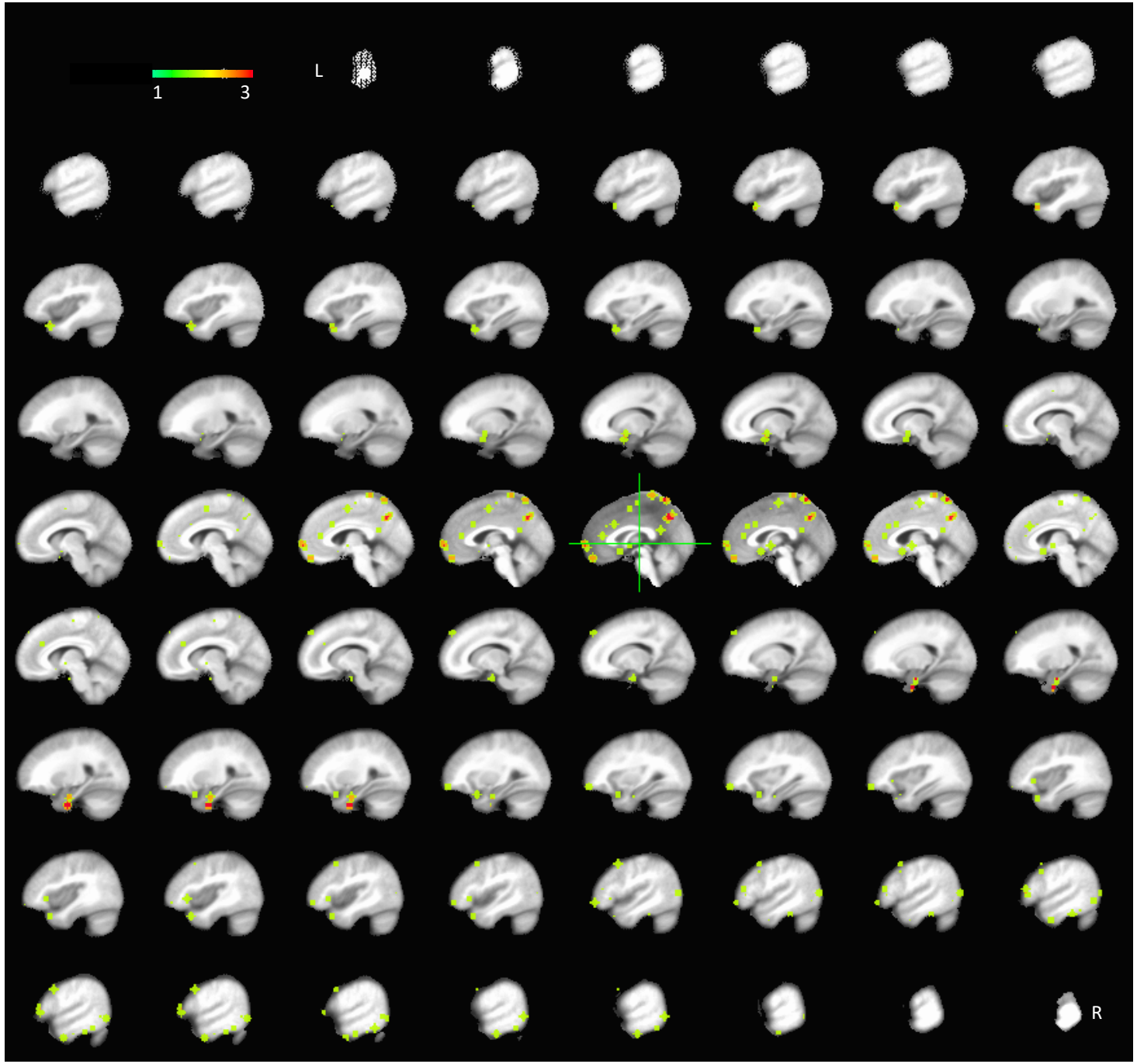

Spatial distribution of ROI masks (each corresponding to the center of mass of an F statistic cluster) identified by 3D ANOVA with a left MTL anchor ROI. 22 anchor ROIs in left hemisphere (*not shown*; see Supplemental Figure 2) comprised the first ("anchor") element in 50 ROI pairs of interest. The spatial distribution of the sum of the ROI masks corresponding to these 50 ROIs is shown.

In this figure, a value greater than one means that this position comprised an ROI pair of interest with more than one anchor MTL ROI.

ANOVA (with correction for multiple hypothesis testing) is used to determine which of the ROI pairs of interest show significant change as an effect of clinical group.

Sagittal plane step size is 2mm. Cross-hair MNI coordinate (0, -18, 0).

Supplemental Figure 4. Grajski & Bressler. 2018.

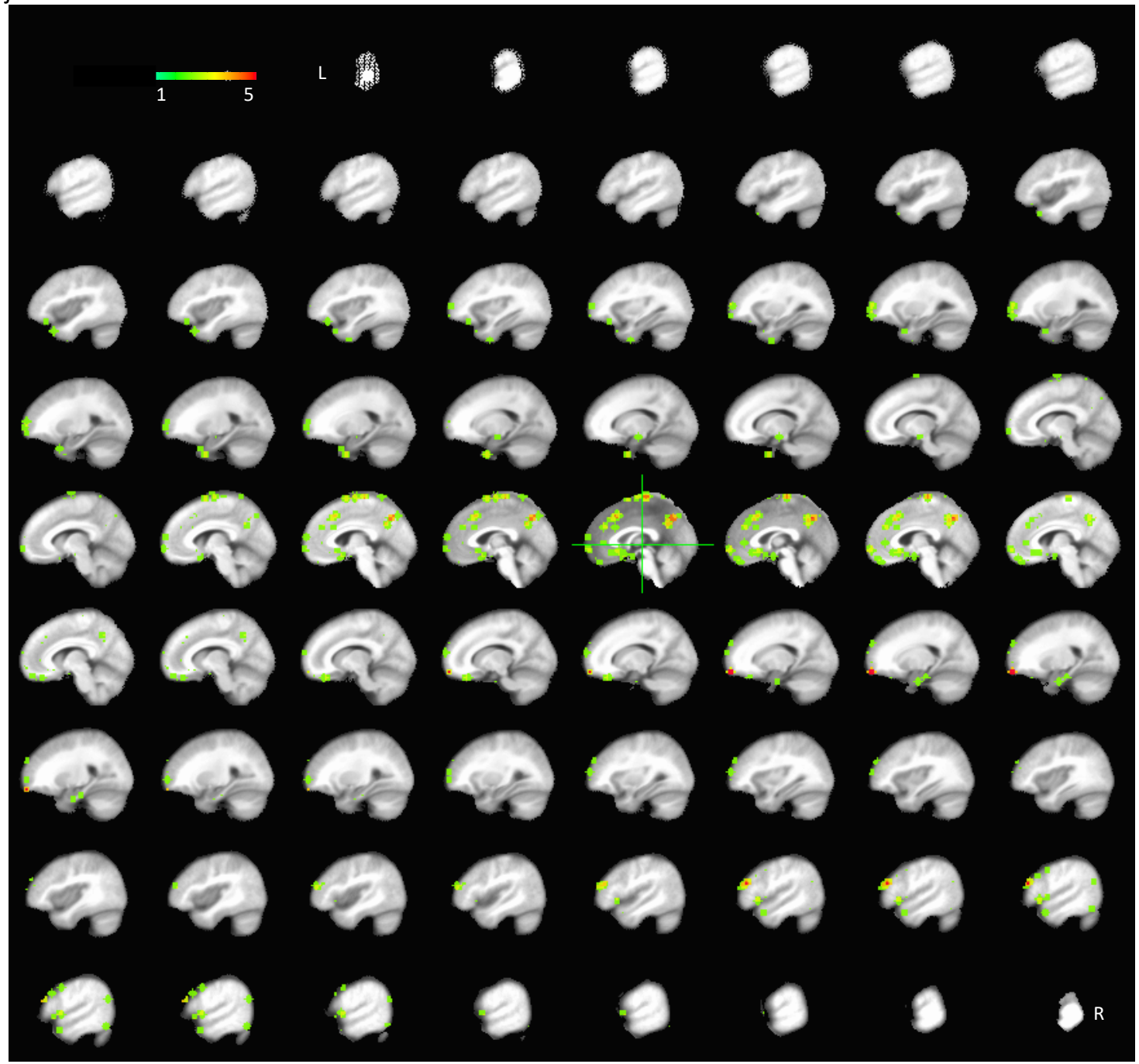

Spatial distribution of ROI masks (each corresponding to the center of mass of an F statistic cluster) identified by 3D ANOVA with a left MTL anchor ROI. 38 anchor ROIs in right hemisphere (*not shown*; see Supplemental Figure 2) comprised the first ("anchor") element in 82 ROI pairs of interest. The spatial distribution of the sum of the ROI masks corresponding to these 82 ROIs is shown.

In this figure, a value greater than one means that this position comprised an ROI pair of interest with more than one anchor MTL ROI.

ANOVA (with correction for multiple hypothesis testing) is used to determine which of the ROI pairs of interest show significant change as an effect of clinical group.

Sagittal plane step size is 2mm. Cross-hair MNI coordinate (0, -18, 0).

Supplemental Figure 5. Grajski & Bressler. 2018.

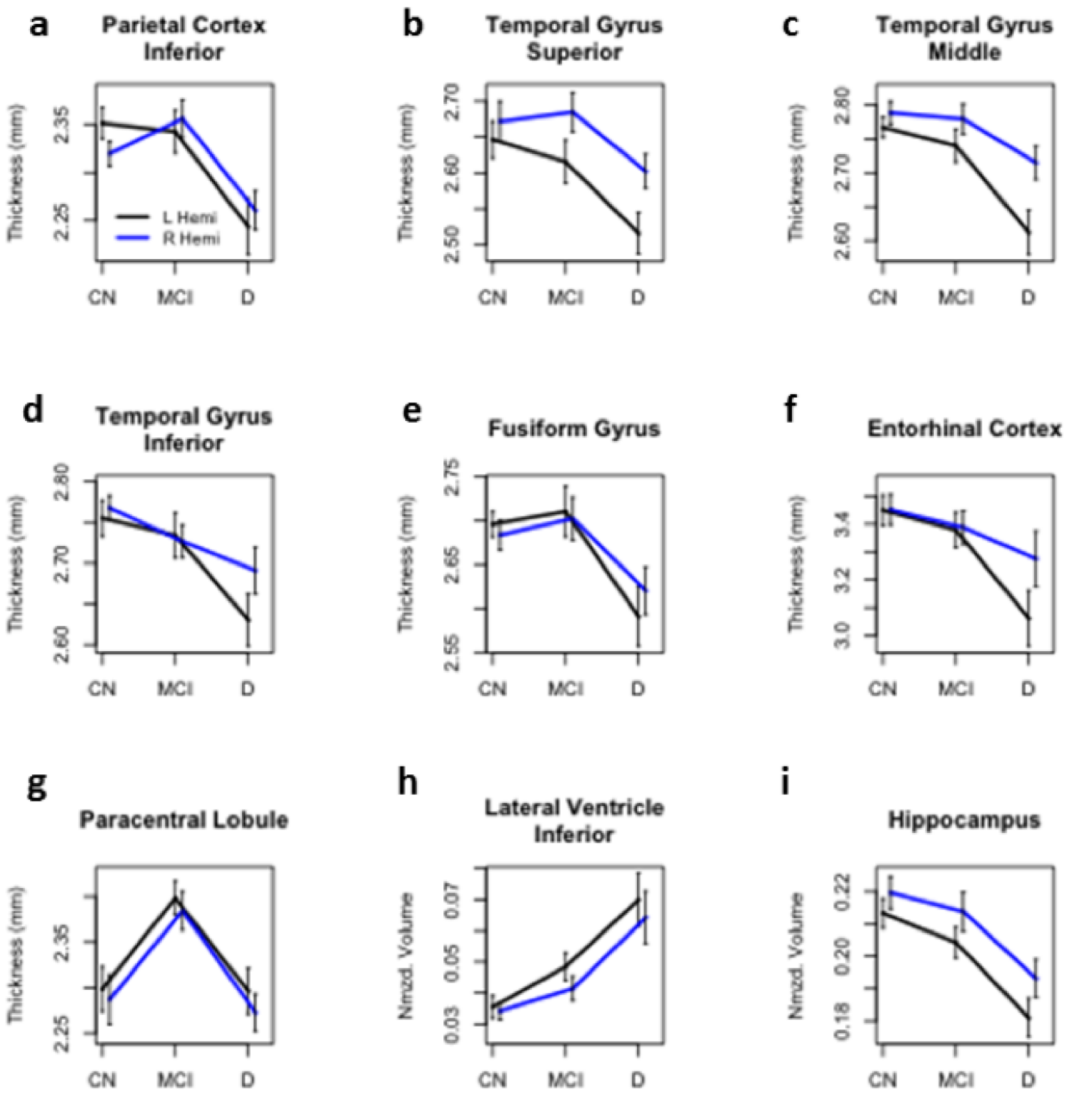

Representative progression of cortical thinning and subcortical structure volume changes with clinical group. ***(a-g)*:** Representative left and right hemisphere CN, MCI and D diagnosis group average and standard error of FreeSurfer 6.0 estimates of labelled regional cortical layer thickness where one or both hemispheres were significant in a one-way, three-factor (CN, MCI, D), ANOVA, FDR-corrected (q=0.1, 68 tests). ***(h-i)*:** Representative left and right hemisphere CN, MCI and D clinical group average and standard error of FreeSurfer 6.0 estimates of labelled subcortical structure volume where one or both hemispheres were significant in a one-way, three-factor (CN, MCI, D), ANOVA, FDR-corrected (q=0.1, 16 tests).

Supplemental Figure 6. Grajski & Bressler. 2018.

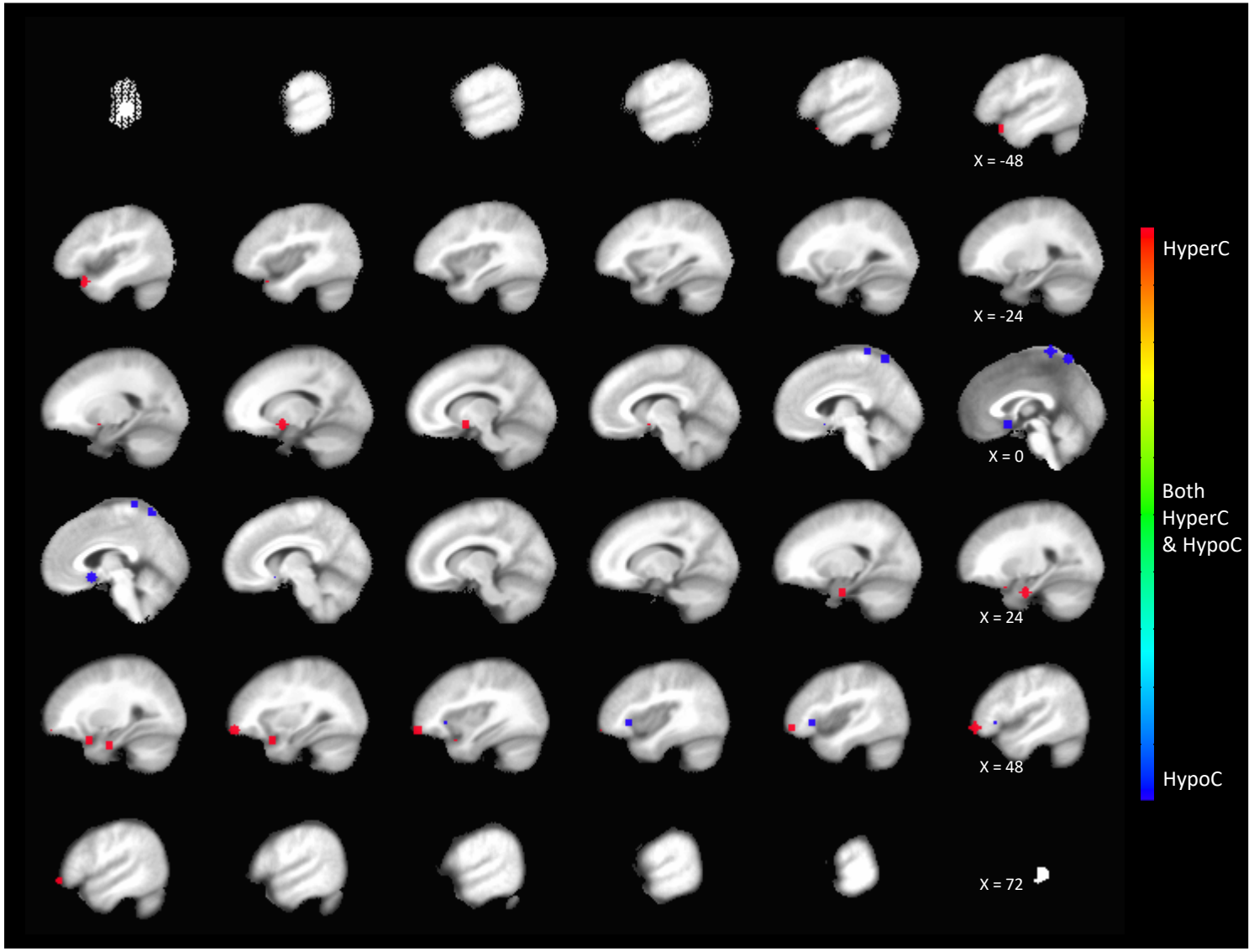

Position of ROI pair of interest non-anchor elements in 10 ROI pairs of interest that were significant in the left hemisphere MCI–CN contrast. The anchor ROIs were in left MTL. Shown are ROI masks consisting of a 6-mm radius volume centered at the ROI seed.

Direction of ROI pair functional change is color-coded for hyperconnected (hyperC) (*red*), hypoconnected (hypoC) (*blue*), and hyperconnected and hypoconnected (*green*).

Supplemental Figure 7. Grajski & Bressler. 2018.

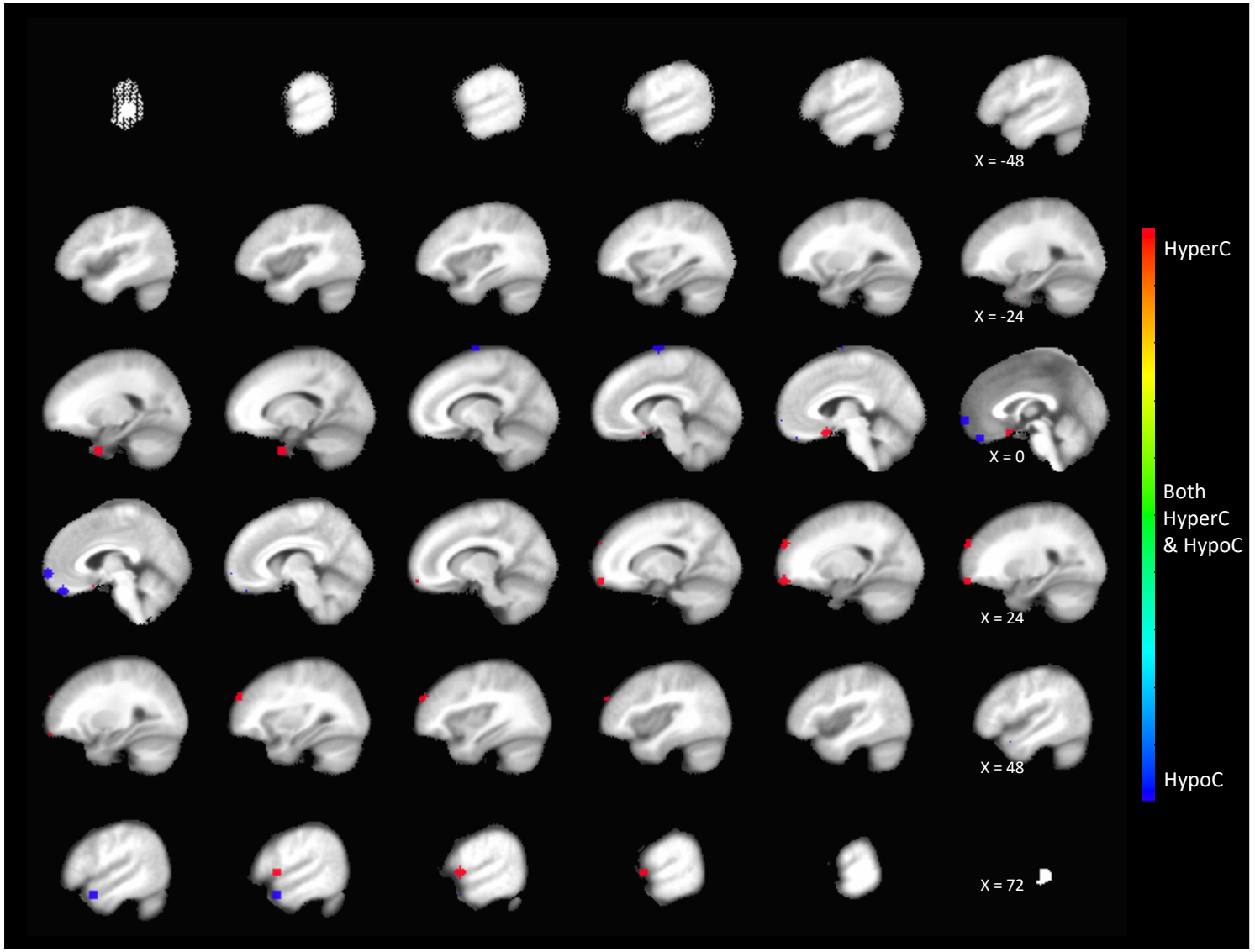

Position of ROI pair of interest non-anchor elements in 13 ROI pairs of interest that were significant in the right hemisphere MCI–CN contrast. The anchor ROIs were in right MTL. Shown are ROI masks consisting of a 6-mm radius volume centered at the ROI seed.

Direction of ROI pair functional change is color-coded for hyperconnected (hyperC) (*red*), hypoconnected (hypoC) (*blue*), and hyperconnected and hypoconnected (*green*).

Supplemental Figure 8. Grajski & Bressler. 2018.

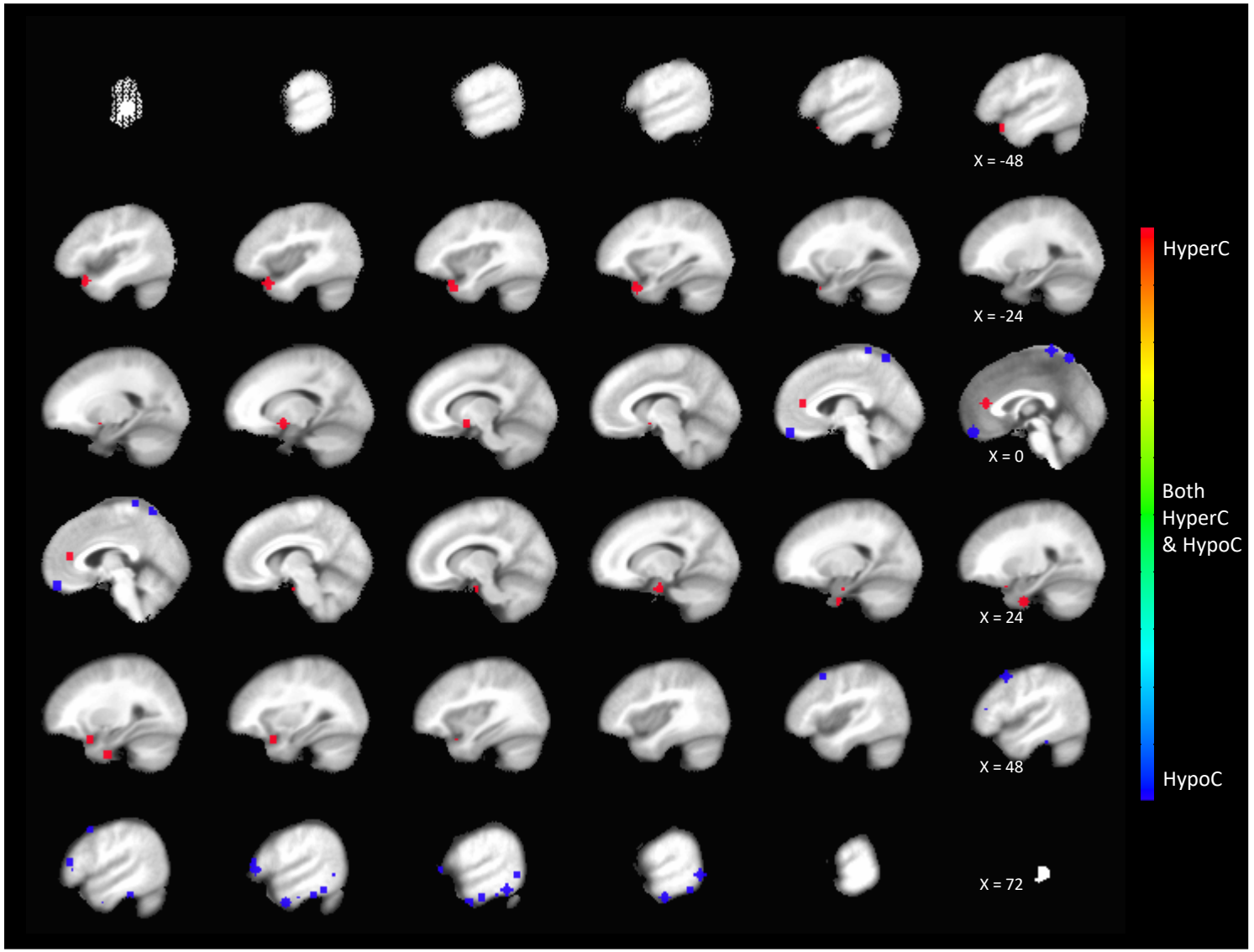

Position of ROI pair of interest non-anchor elements in 21 ROI pairs of interest that were significant in the left hemisphere AD–CN contrast. The anchor ROIs were in left MTL. Shown are ROI masks consisting of a 6-mm radius volume centered at the ROI seed.

Direction of ROI pair functional change is color-coded for hyperconnected (hyperC) (*red*), hypoconnected (hypoC) (*blue*), and hyperconnected and hypoconnected (*green*).

Supplemental Figure 9. Grajski & Bressler. 2018.

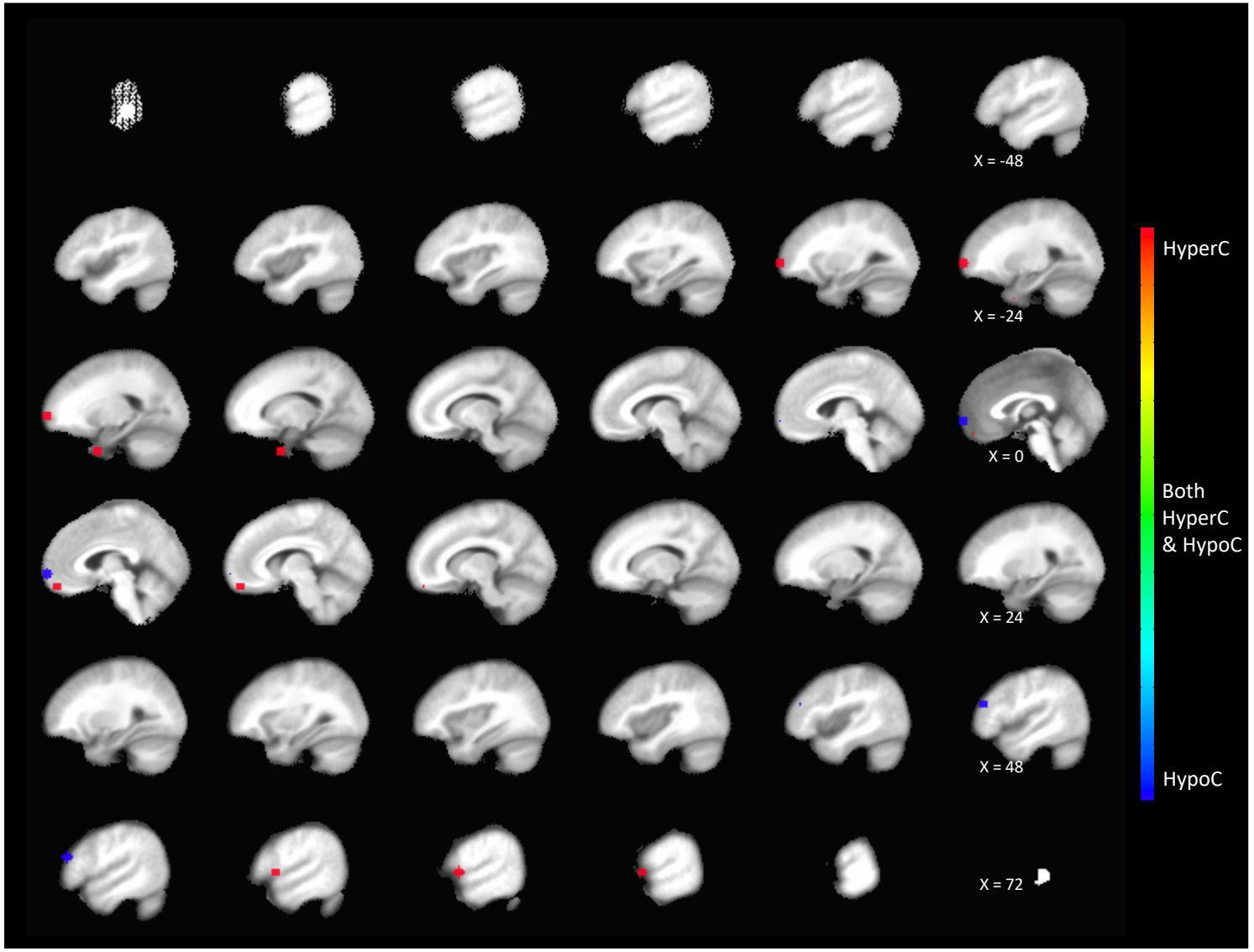

Position of ROI pair of interest non-anchor elements in 6 ROI pairs of interest that were significant in the right hemisphere AD–CN contrast. The anchor ROIs were in right MTL. Shown are ROI masks consisting of a 6-mm radius volume centered at the ROI seed.

Direction of ROI pair functional change is color-coded for hyperconnected (hyperC) (*red*), hypoconnected (hypoC) (*blue*), and hyperconnected and hypoconnected (*green*).